Supporting Information

Phosphorization-Pyrolysis Engineered FeP@CNT Heterostructures for Efficient and Durable Direct Seawater Electrolysis

Samikannu Prabu[a,1], Giwon Lee[b,1], Mohan Reddy Pallavolu[c], Jinhan Cho[d], Yong Nam Ahn[a,*], Sungjun Park[e,f,*], Daegun Kim[a,*]

[a] School of Chemical, Biological and Battery Engineering, Gachon University, 13120 Seongnam, Republic of Korea.
[b] Department of Chemical Engineering, Kwangwoon University, Seoul 01897, Republic of Korea.
[c] School of Chemical Engineering, Yeungnam University, Gyeongsan, 38541, Republic of Korea.
[d] Department of Chemical and Biological Engineering, Korea University, Seoul 02841 Republic of Korea.
[e] Department of Electrical and Computer Engineering, Ajou University, Suwon 16499, Republic of Korea.
[f] Department of Intelligence Semiconductor Engineering, Ajou University, Suwon 16499, Republic of Korea.
E-mail: sj0223park@ajou.ac.kr

* Corresponding authors.
E-mail addresses : yahn@gachon.ac.kr (Y. N. Ahn), sj0223park@ajou.ac.kr (S. Park), daegunkim@gachon.ac.kr (D. Kim)

[1] The authors contributed equally to this work.

1. Experimental section

1.1. Chemicals

Iron nitrate hexahydrate ($Fe(NO_3)_2 \cdot 6H_2O \geq 99\%$, Sigma-Aldrich), zinc nitrate hexahydrate ($Zn(NO_3).6H_2O$, Sigma-Aldrich, ≥98.0%), Potassium hydroxide (KOH, ACS reagent, ≥85%, pellets), hydrochloric acid (HCl, Alfa Aesar, 38%). Sodium phosphate monobasic (NaH_2PO_4, *ReagentPlus*®, ≥99.0%, Merck). Natural seawater was collected from Chu-wei Beach, Zhongli, Taiwan. Ni-foam (NF) was obtained from Clean Energy Technology CO., LTD. The water used throughout all experiments was purified through a Millipore system.

1.2. Preparation method of coated electrode

The active material, polytetrafluoroethylene (PTFE), and acetylene black were mixed in a mass ratio of 8:1.5:0.5. The components were first thoroughly ground using an agate mortar to obtain a homogeneous mixture. Subsequently, an appropriate amount of N-methyl-2-pyrrolidone (NMP) was added to form a uniform slurry. The resulting slurry was then evenly coated onto a 1 × 1 cm^2 nickel foam (Ni foam) substrate and dried in a vacuum oven at 60 °C until completely dry, after which the electrode was used for electrochemical measurements.

The Pt/C and RuO_2 benchmark electrodes were prepared using a conventional catalyst coating method. Briefly, the commercial Platinum on carbon (Pt/C, 20 wt%) and Ruthenium dioxide (RuO_2) catalysts were used as received. For each catalyst, 5 mg of powder was dispersed in a mixed solvent containing 950 μL of ethanol and 50 μL of Nafion solution (5 wt%). The suspension was ultrasonicated for 30 min to obtain a homogeneous catalyst ink. Subsequently, an appropriate amount of the ink (typically 10-20 μL) was drop-cast onto a 1 × 1 cm^2 nickel foam substrate and

dried at 60 °C in an oven to remove the solvent. The resulting electrodes were used directly as reference catalysts for electrochemical measurements.

1.3. Electrochemical characterization

Electrochemical HER and OER experiments were performed using the CHI 6273B electrochemical workstation, with the above-mentioned samples, a Pt wire, and an Ag/AgCl electrode as the working electrode, counter electrode, and reference electrode, respectively. The water-splitting performance of the electrolytes was tested in a two-electrode system, where OER electrodes are the anode, and HER electrodes are the cathode. Three different electrolytes, including 1 M KOH + seawater and 1.0 M KOH, were used, and the pH was about 13.8. All measured potentials were referenced to that of the reversible hydrogen electrode (RHE) (E_{RHE}) = $E_{Ag/AgCl}$ + 0.059 * pH + 0.197 V. Electrochemical impedance spectroscopy (EIS) measurements were performed at open-circuit potentials between 110 and 0.01 Hz with an amplitude of 5 mV. The catalytic activity of the catalysts was determined by linear sweep voltammetry (LSV) curves with a scan rate of 5 mV s^{-1}. The double-layer capacitance (C_{dl}) values were obtained via cyclic voltammetry (CV) curves with scan rates of 10-200 mV s^{-1}. All data have been reported with 90 % i*R* compensation. The i*R*-compensated potential was obtained after the correction of solution resistance measured following the equation: $E_{corr} = E - iR$, where E is the original potential, R is the solution resistance, i is the corresponding current, and E_{corr} is the i*R*-compensated potential.

The ECSA was calculated using the equation:

$$C_{dl}/Cs,$$

where Cs is the specific capacitance of a flat, smooth surface, typically taken as 0.040 mF cm^{-2} in 1 M KOH electrolyte.

H_2 and O_2 gases were collected using a gas-tight system during galvanostatic electrolysis under the same conditions used for the electrochemical measurements. Gas volumes were recorded at regular intervals, and the Faradaic efficiency was calculated by comparing the experimentally measured gas volumes with the theoretical values obtained from the total charge passed based on Faraday's law. The measured gas evolution closely matched the theoretical values, confirming nearly 100% Faradaic efficiency and high charge utilization for overall water splitting.

The Faradaic efficiency (FE) is then calculated as:

$$FE(\%)=\frac{n_{exp}}{n_{theo}} \times 100$$

where n_{exp} is the experimentally measured amount of gas and n_{theo} is the theoretical amount calculated from Faraday's law.

1.4. Solar-driven seawater electrolysis test

The solar-driven electrolysis experiment was performed using a commercial photovoltaic (PV) cell as the power source. The PV cell delivered an open-circuit voltage of approximately 3 V, which was directly connected to the two-electrode electrolyzer containing the prepared catalysts. The electrolysis cell was operated using the alkaline seawater electrolyte under natural sunlight illumination. During the test, the ambient temperature was approximately 28 °C, and the system was continuously operated for 5 h to evaluate the feasibility of solar-driven hydrogen and oxygen generation. The experiment was conducted without additional external bias, and gas evolution from both electrodes was visually monitored during the electrolysis process.

1.5. Characterizations

The crystallographic data were investigated using powder X-ray diffraction (XRD, Bruker D8 Advance) equipped with Cu Kα radiation (λ = 1.5406 Å) at a scanning rate of 5° min^{-1} (40 kV, 20 mA). Microstructure was considered using Transmission Electron Microscopy (TEM, JEM-2010) and High-resolution Transmission Electron Microscopy (HRTEM), prepared with EDX microanalysis and selected area electron diffraction (SAED), and an energy dispersive X-ray detector (EDX) for the elemental analysis to obtain the detailed microstructure information of the synthesized catalysts. The detailed microstructures of the synthesized samples were examined using Field Emission Scanning Electron Microscopy (FESEM, S-800 host of Japanese HITACHI). X-ray photoelectron spectroscopy (XPS) analysis was performed on a Rigaku-NANO-Viewer X-ray photoelectron spectrometer with an achromatized Al Kα source (15 kV, 150 W), and the material surface compositions. The Ar sputtering experiments were carried out in a detailed vacuum environment of 5×10^{-6} Pa and a sputtering accelerating voltage of 3 kV.

1.6. Simulation Details

The first-principles calculations were performed using the density functional theory (DFT) implemented in the Vienna ab-initio simulation package (VASP).[1,2] The Perdew–Burke–Ernzerhof (PBE) version of the generalized gradient approximation (GGA) was adopted for the exchange–correlation functional.[3] The core electrons were incorporated into pseudopotentials using the projector-augmented-wave (PAW) method.[4] A Monkhorst–Pack scheme[5] with a 3 × 3 × 1 k-mesh was used to sample the electronic Brillouin zone, and the plane-wave cutoff energy was set to 520 eV. The energy convergence criterion and residual force at each atom were set to $\leq 10^{-4}$ eV and ≤0.02 eV $Å^{-1}$, respectively.

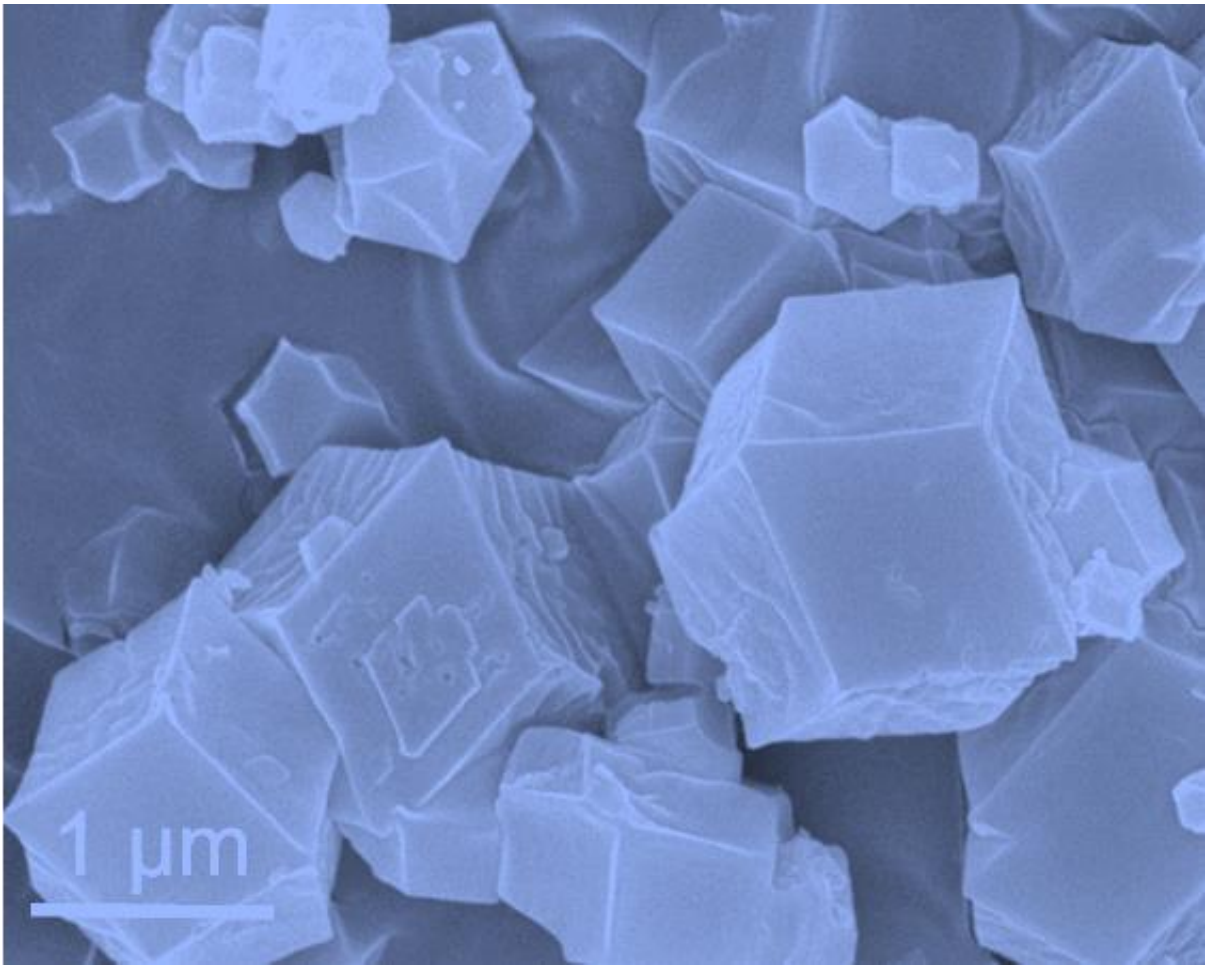

Fig. S1. FE-SEM images of ZnFe-MOF.

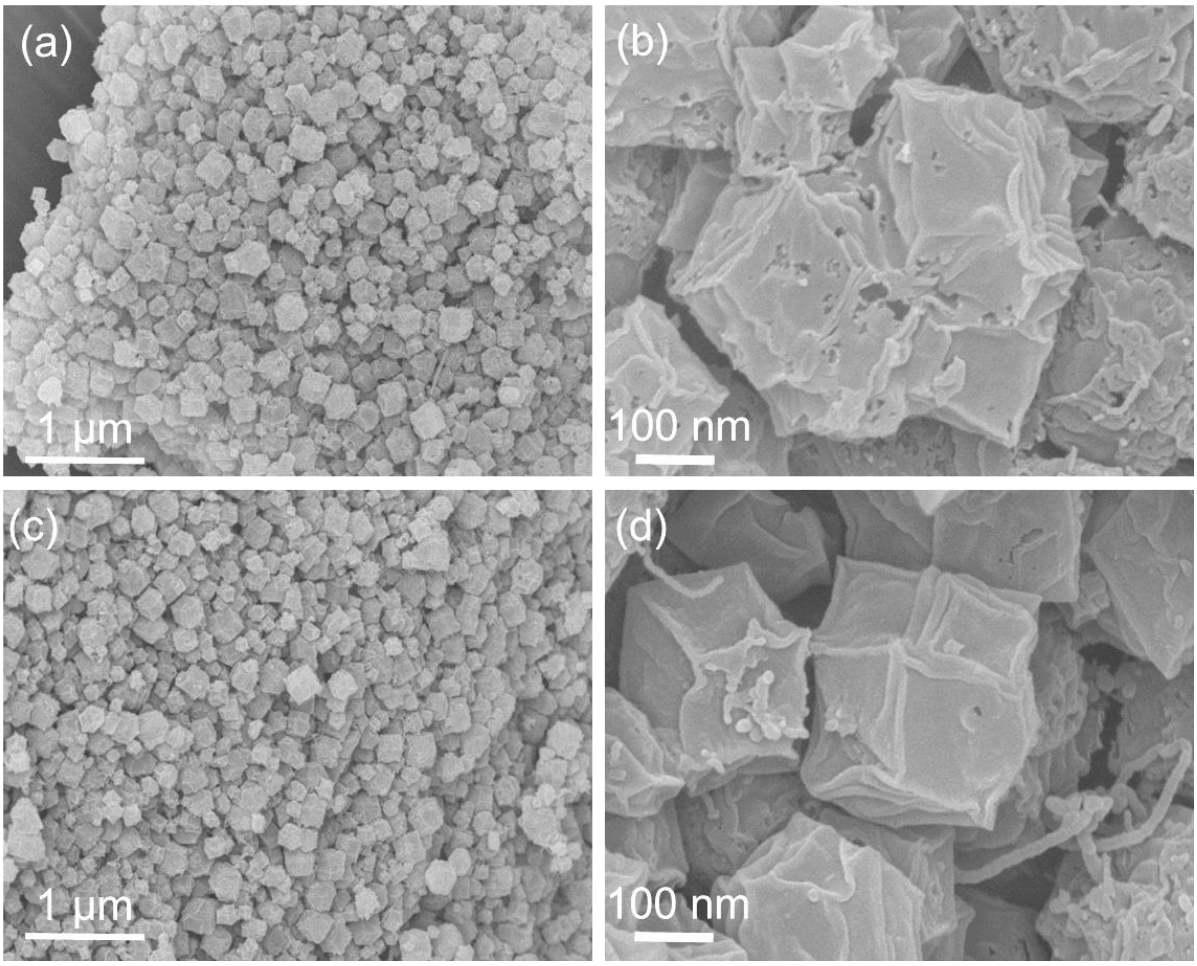

Fig. S2. FE-SEM images of (a,b) 800 ºC and (c,d) 850 ºC during the synthesis of FeP@CNT.

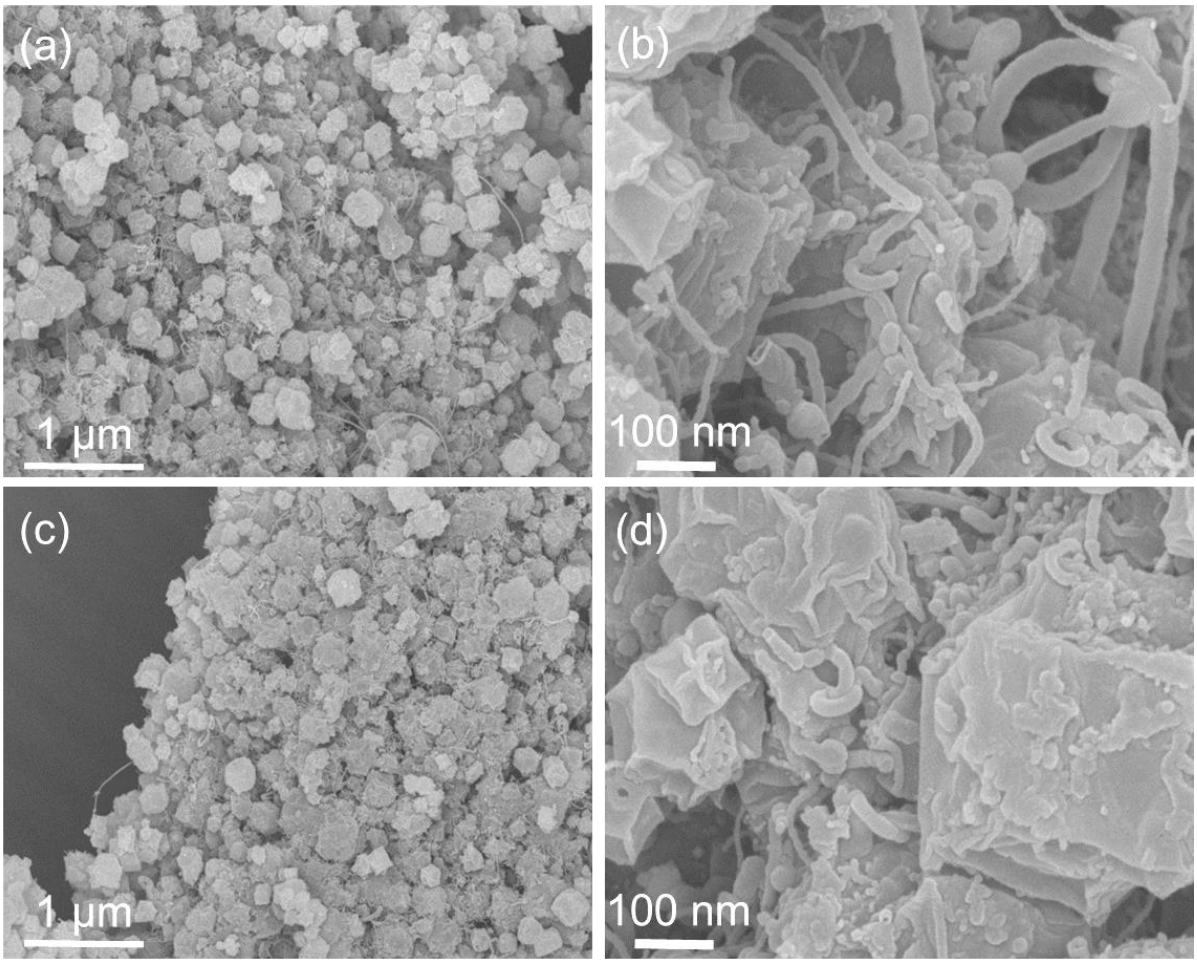

Fig. S3. FE-SEM images of (a,b) 900 ºC and (c,d) 950 ºC during the synthesis of FeP@CNT.

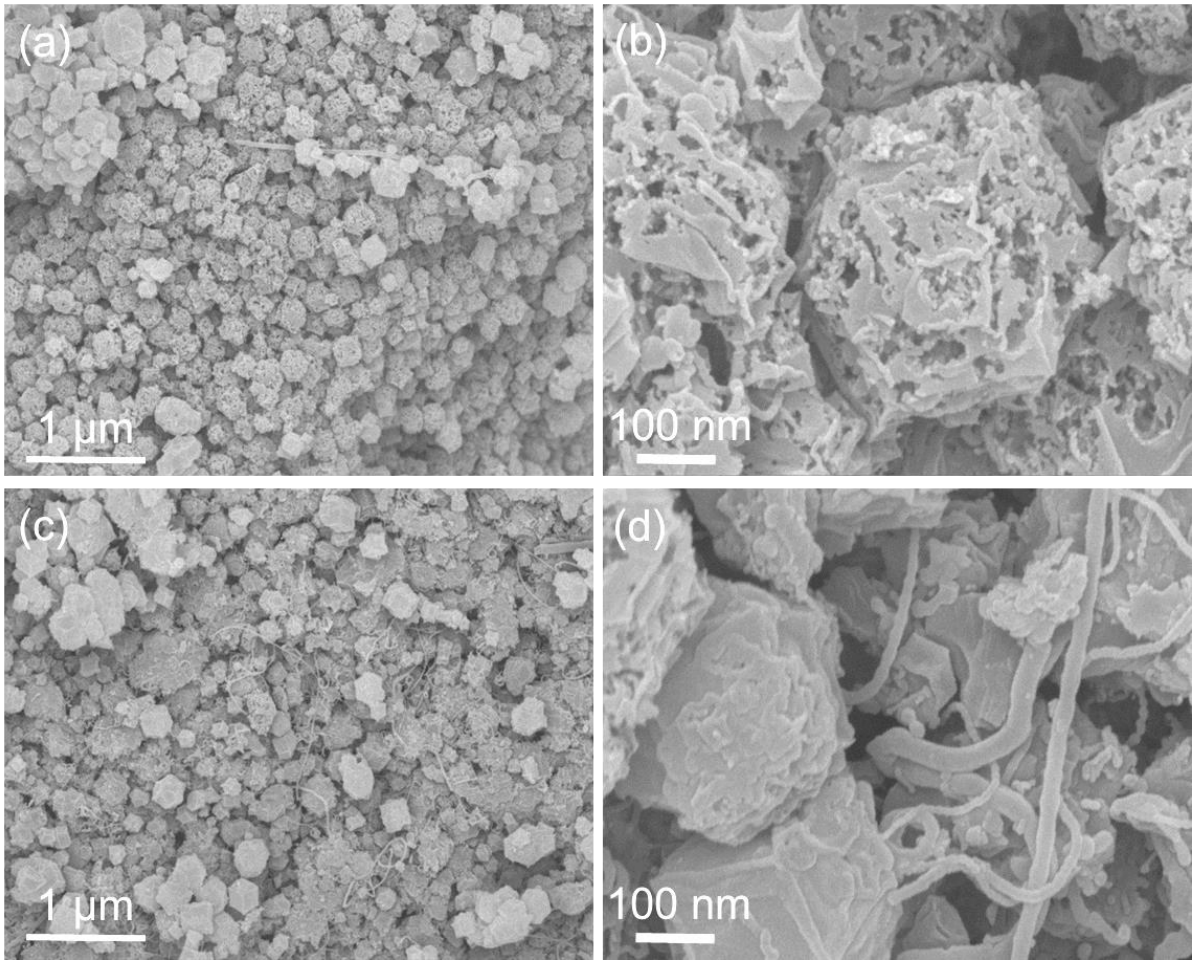

Fig. S4. FE-SEM images of (a,b) 1 wt. and (c,d) 2 wt. of NaH_2PO_4 at 900 ^oC.

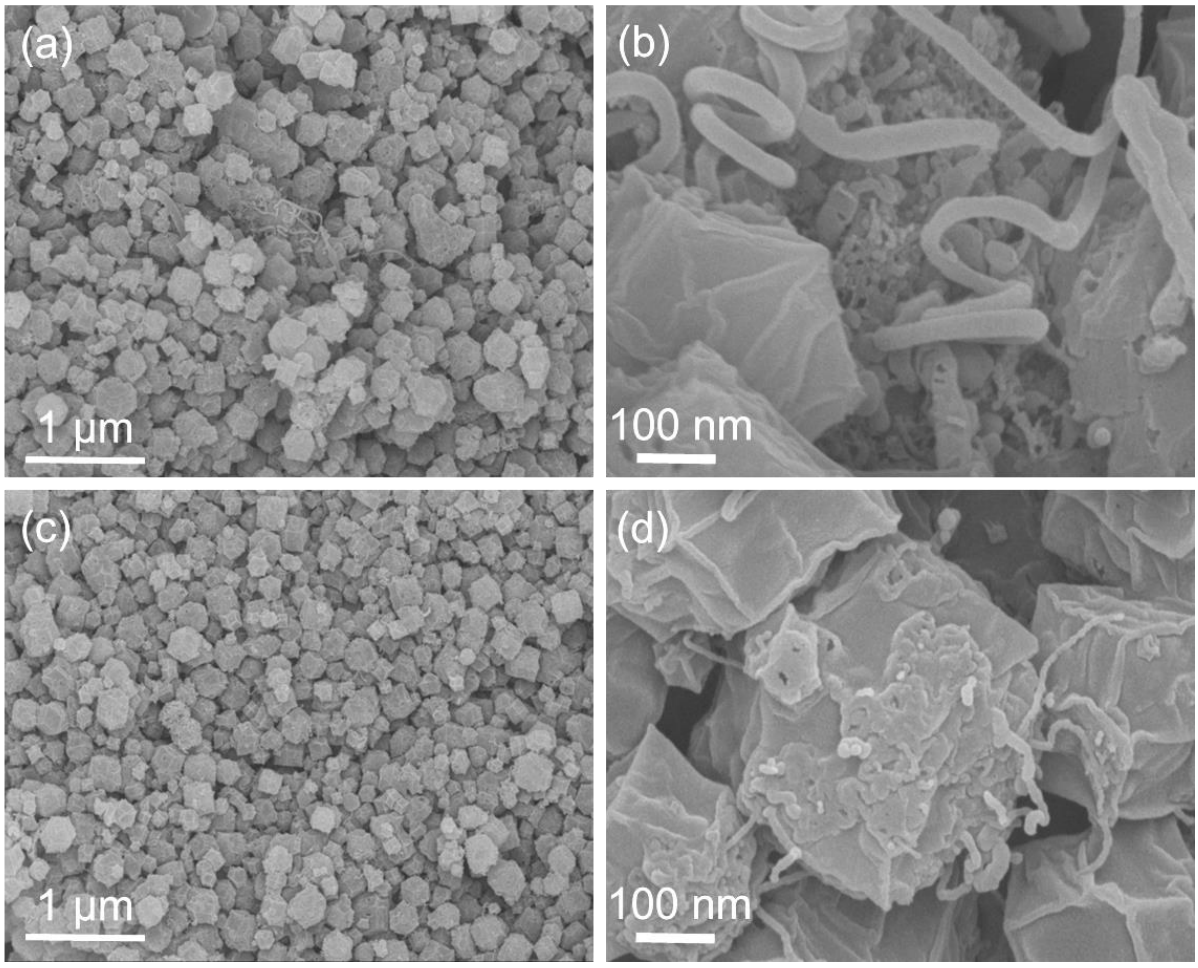

Fig. S5. FE-SEM images of (a,b) 3 wt. and (c,d) 4 wt. of NaH_2PO_4 at 900 ºC.

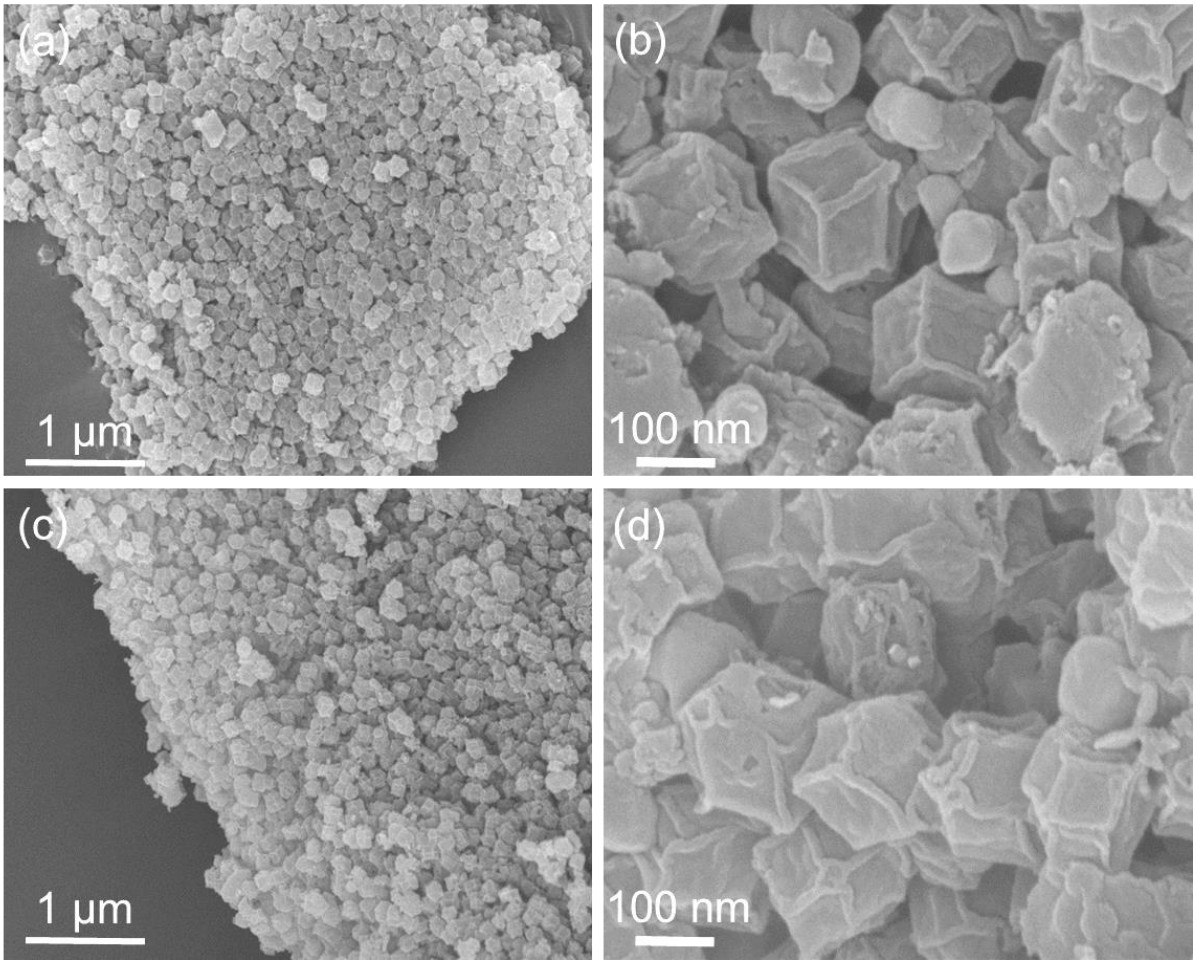

Fig. S6. FE-SEM images of (a,b) Fe@800 and (c,d) Fe-900.

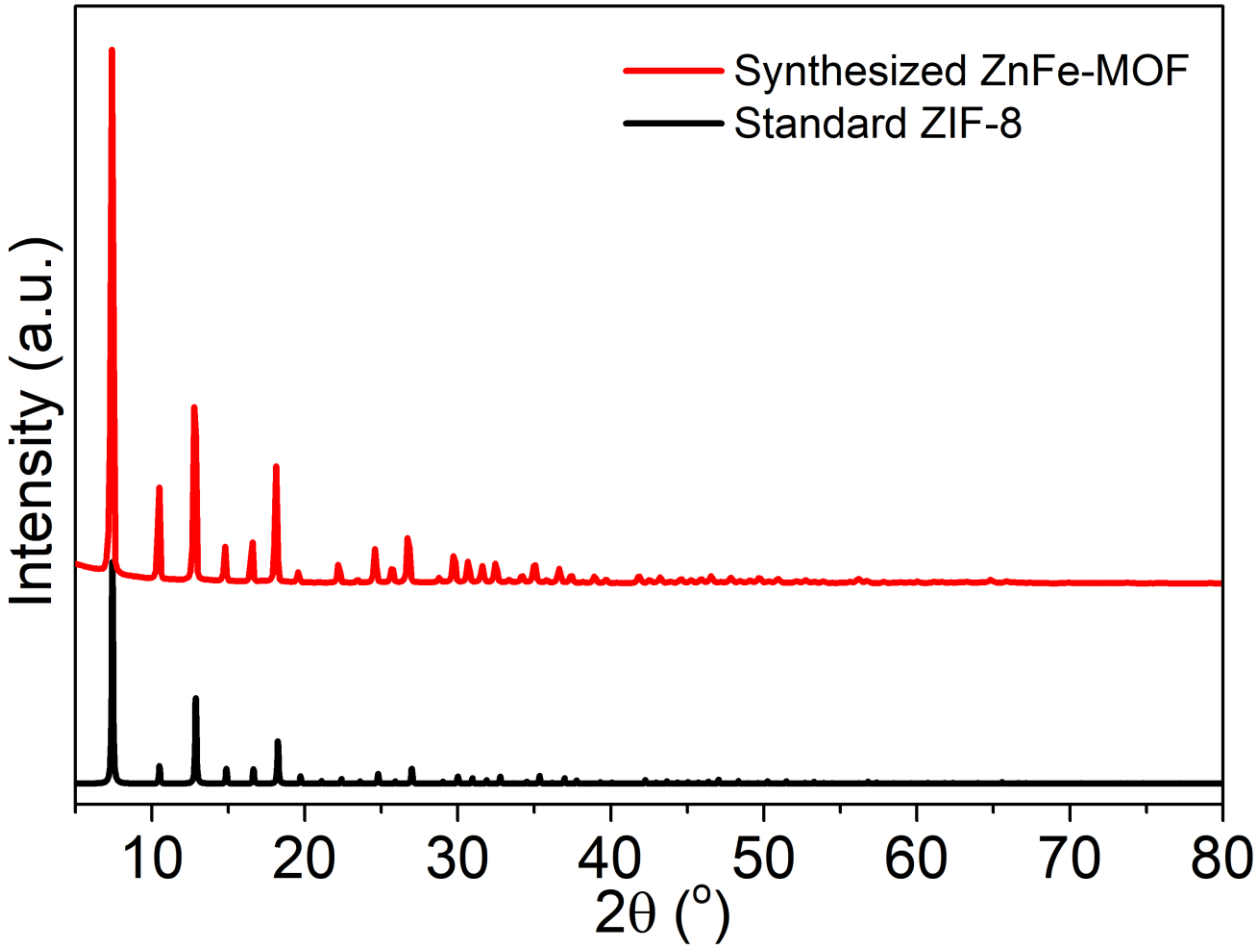

Fig. S7. XRD pattern of synthesized ZnFe-MOF.

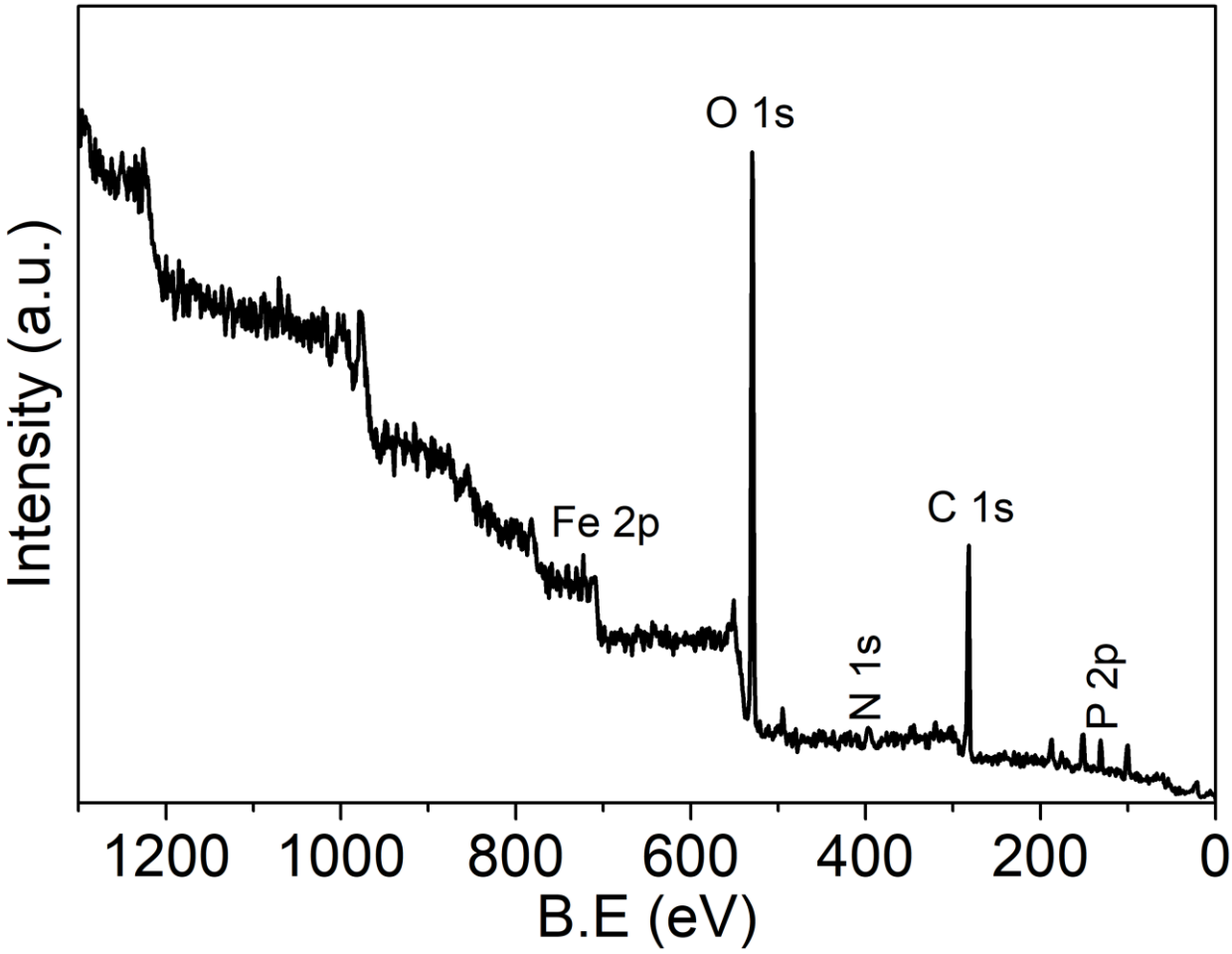

Fig. S8. XPS full survey spectra of FeP@CNT-900-2

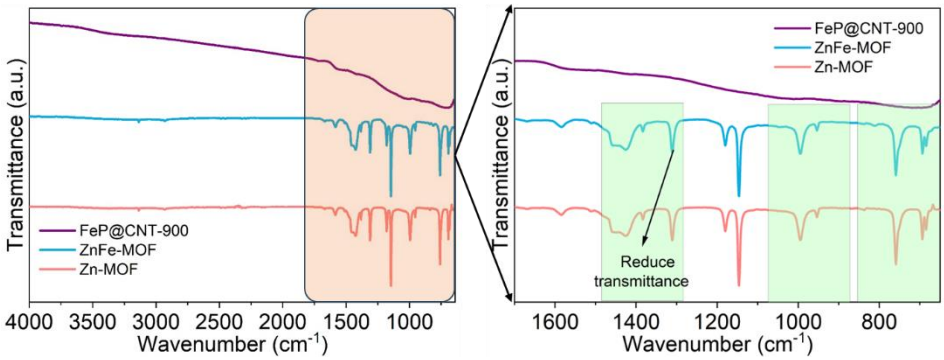

Fig. S9. FTIR spectra of Zn-MOF, ZnFe-MOF and FeP@CNT-900-2.

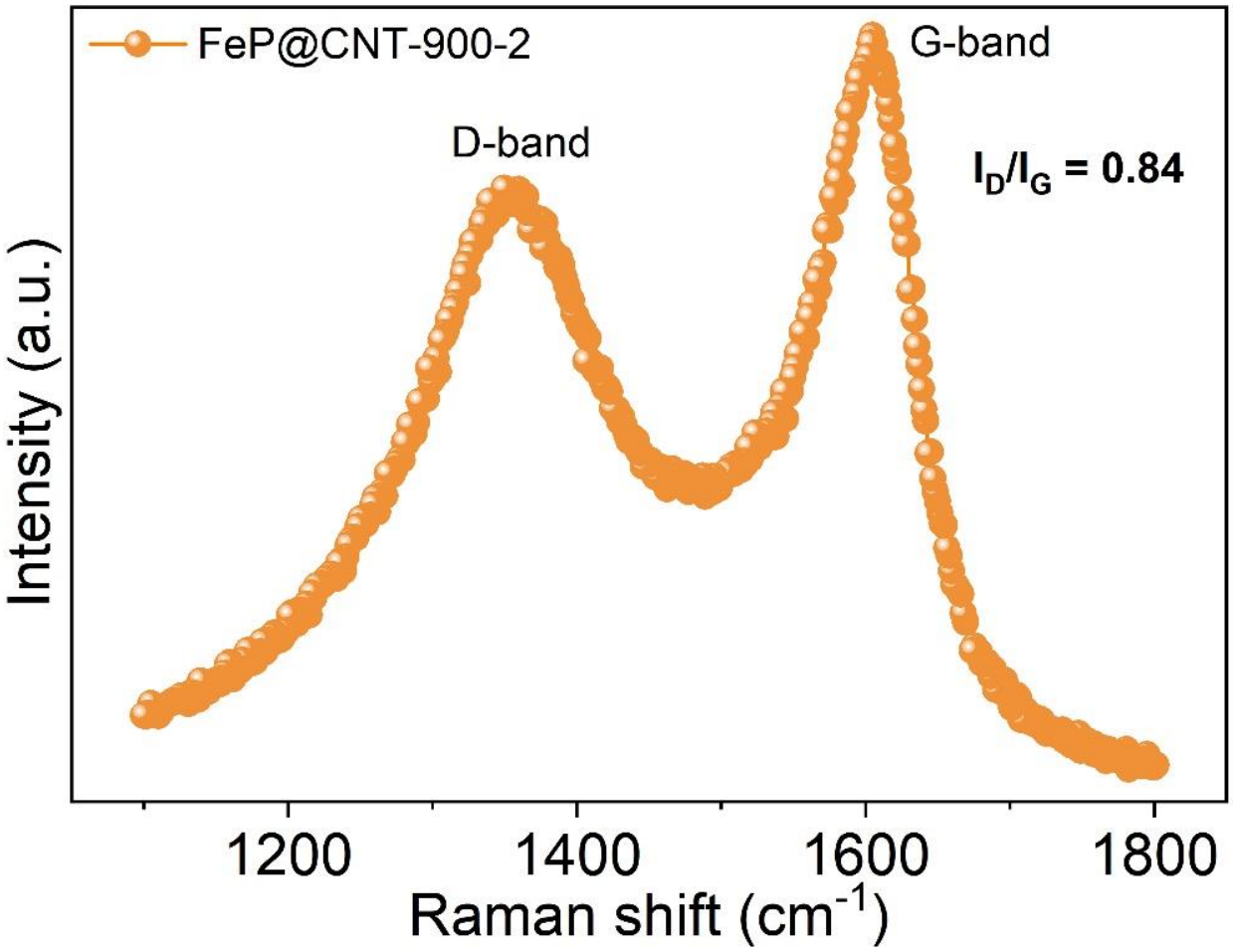

Fig. S10. Raman spectra of FeP@CNT-900-2 catalysts.

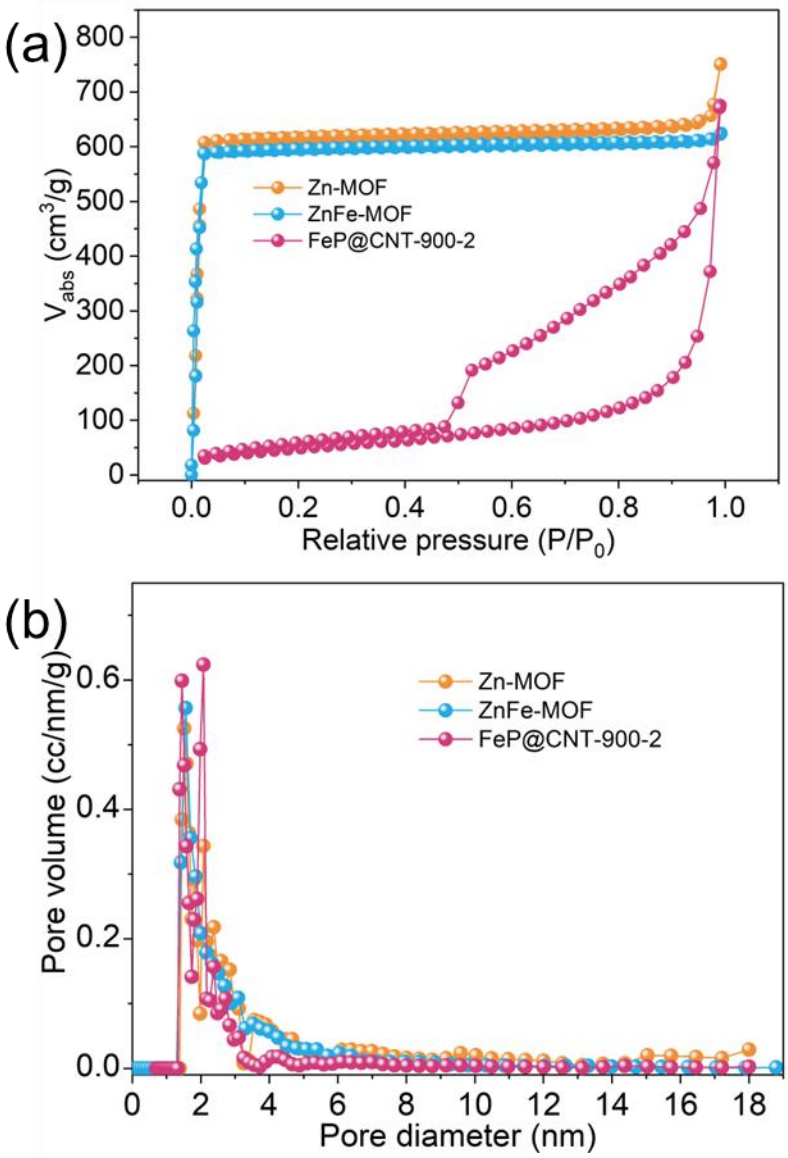

Fig. S11. BET and (d) Pore volume and pore size of the prepared different materials (Zn-MOF, ZnFe-MOF, and FeP@CNT-900-2).

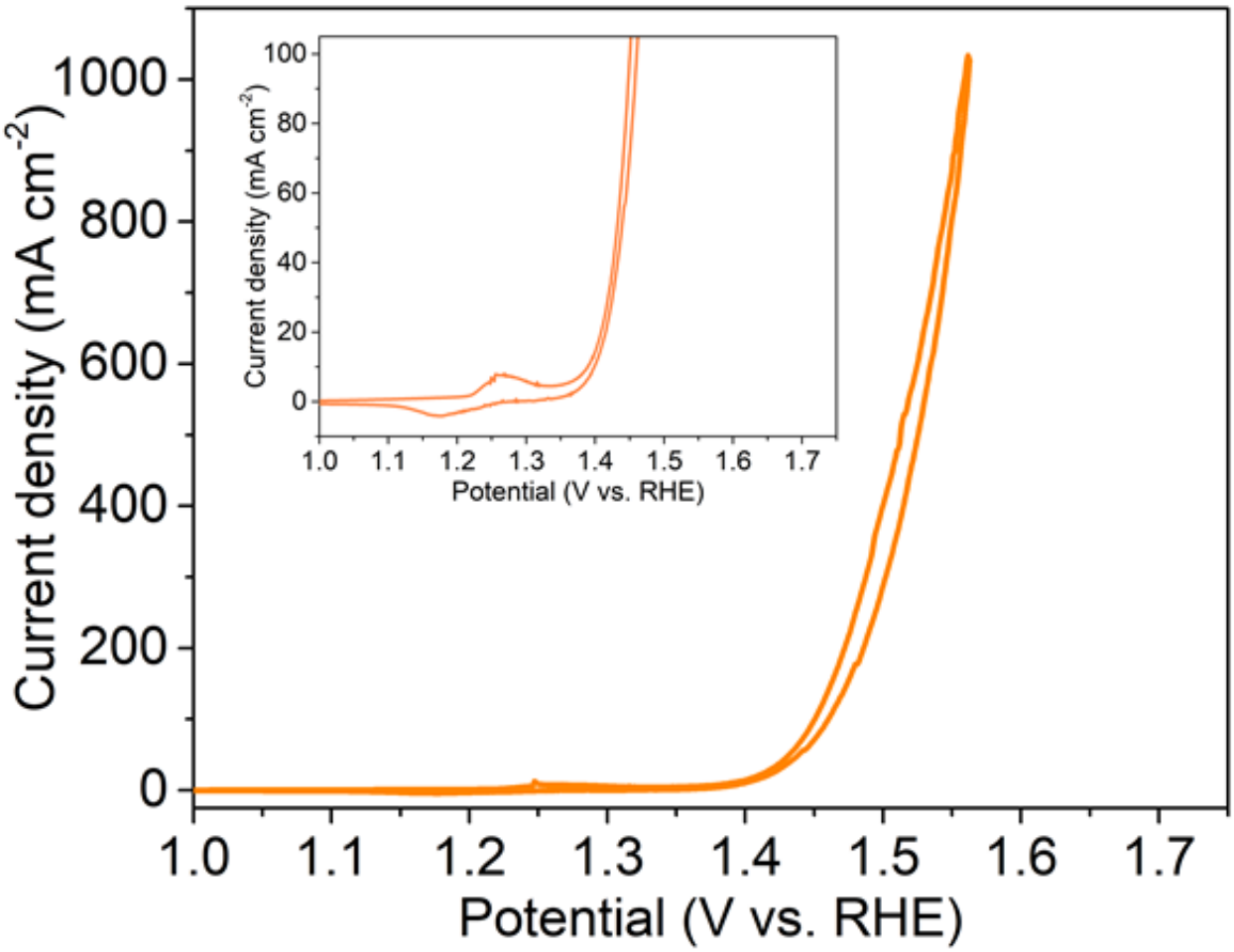

Fig. S12. CV curve of FeP@CNT-900-2 at a scan rate of 5 mV s^{-1}. A low scan rate can reduce signal overlap between $Fe^0/Fe^{2+}/Fe^{3+}$ oxidation and OER activity.

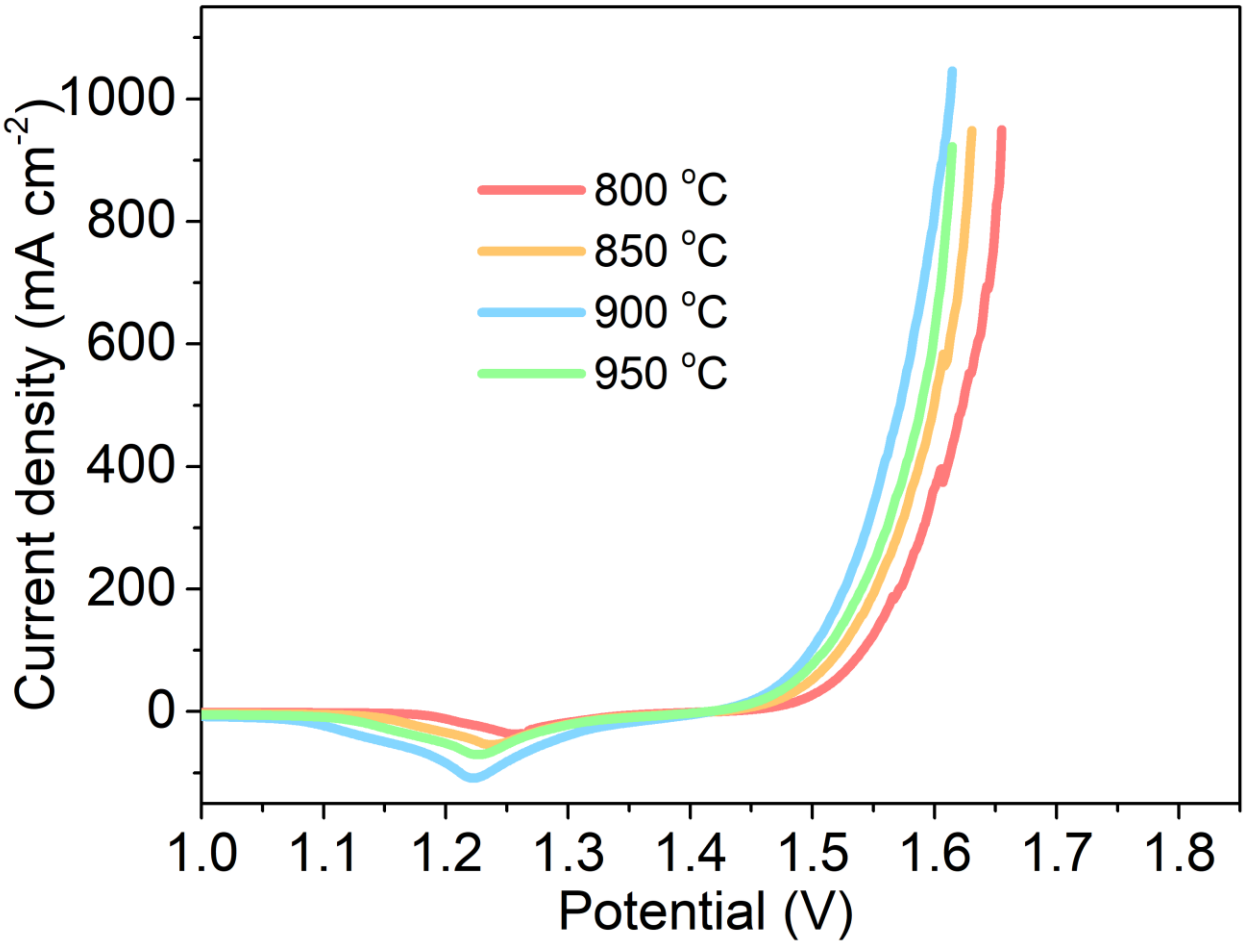

Fig. S13. LSV OER curves of FeP@CNT electrodes fabricated at different temperatures in alkaline seawater.

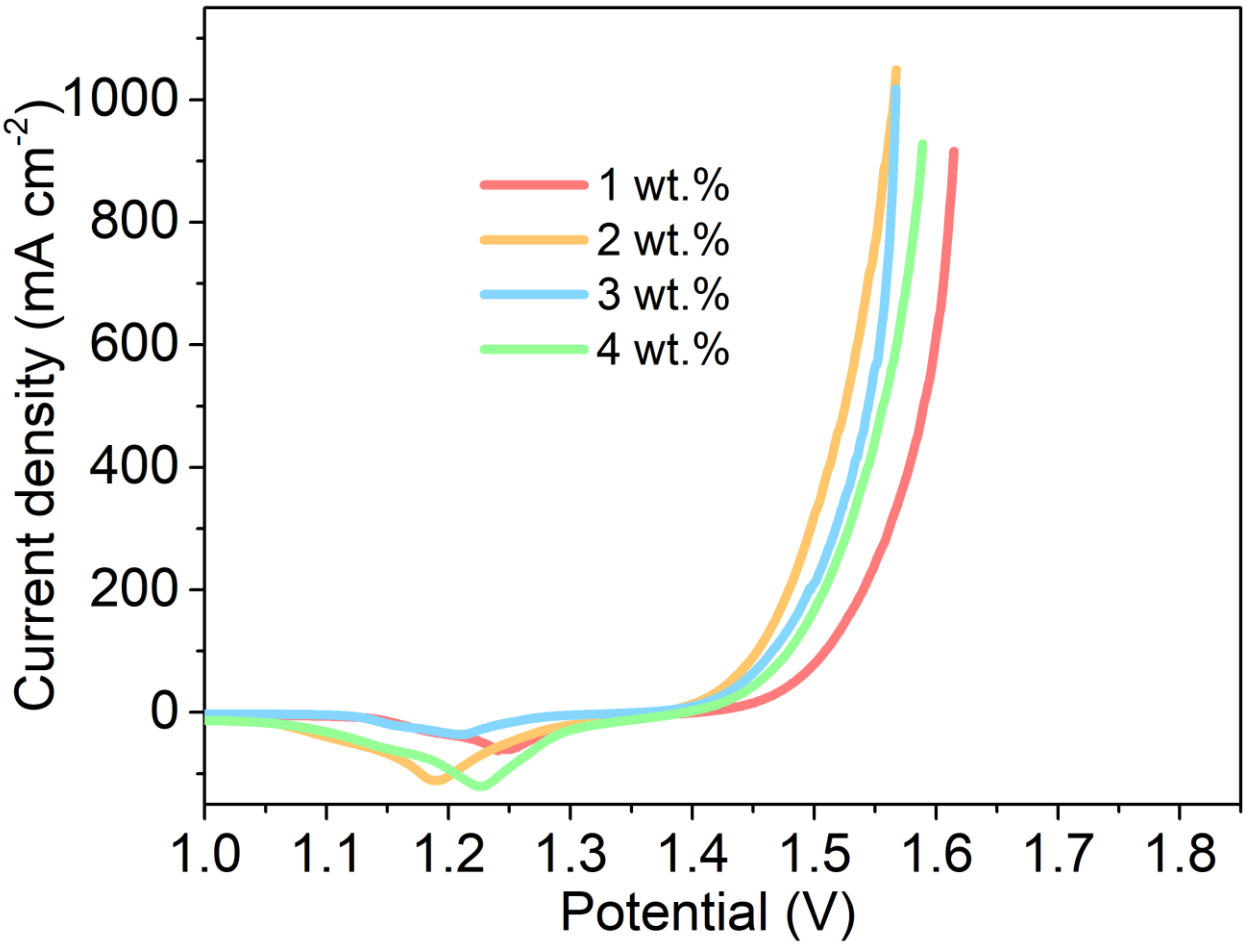

Fig. S14. LSV curves of FeP@CNT electrodes fabricated at different wt.% of NaH_2PO_4.

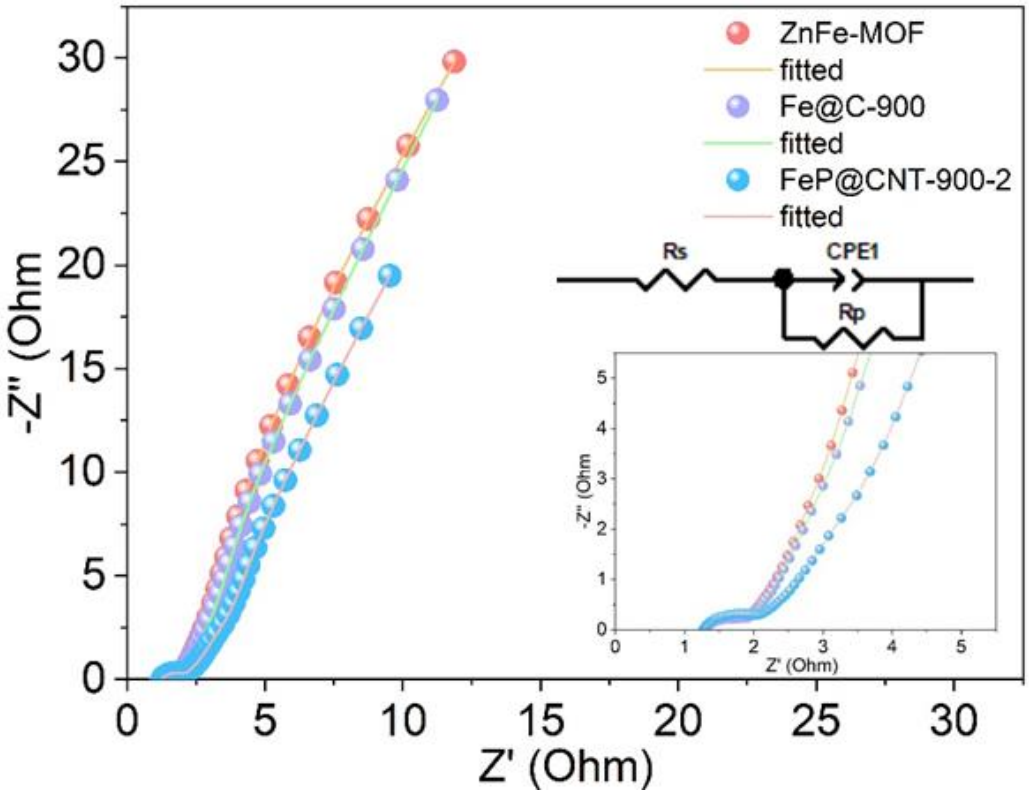

Fig. S15. EIS spectra of various electrode materials in alkaline seawater for the OER.

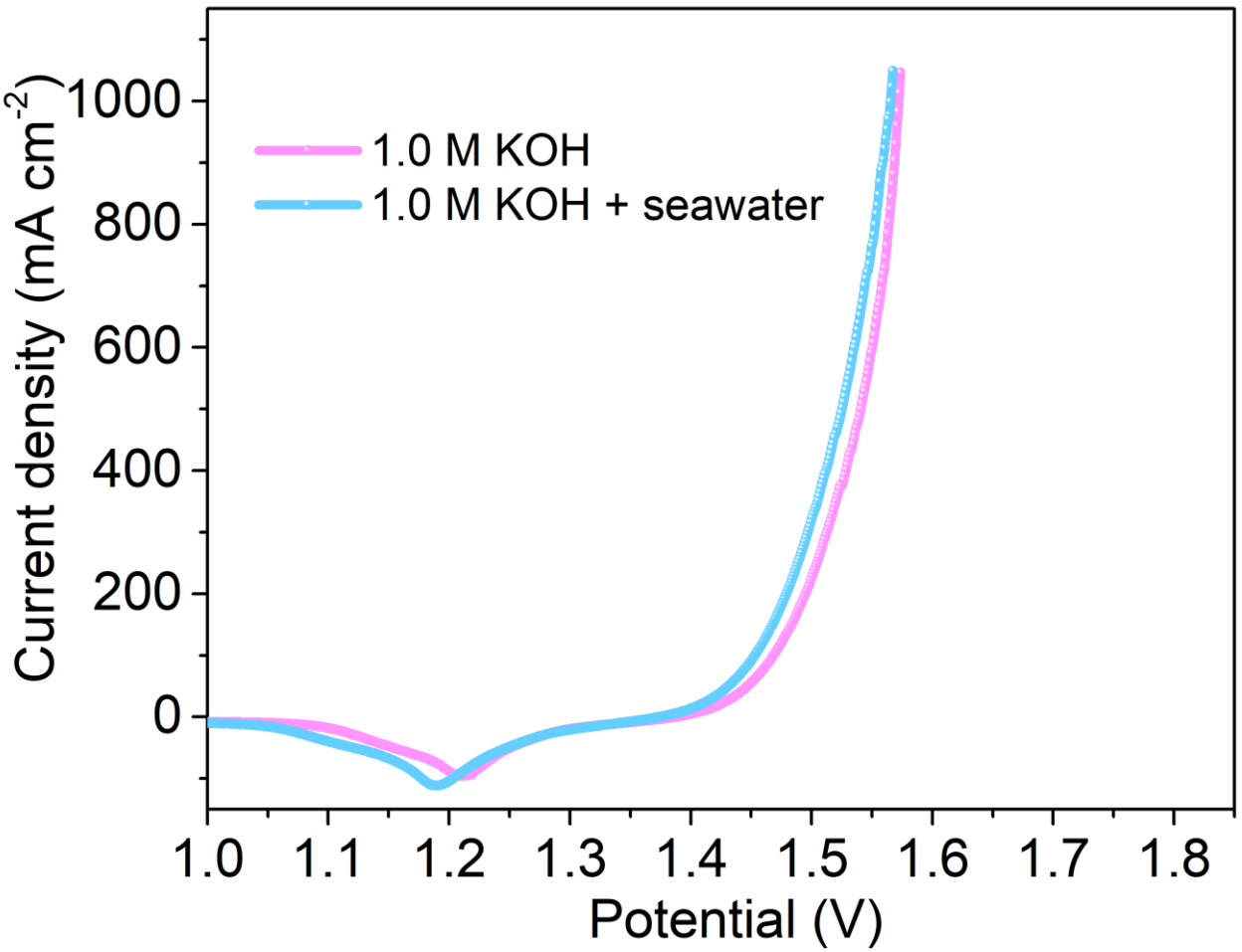

Fig. S16. LSV curves of FeP@CNT-900-2 in the electrolytes of 1.0 M KOH and 1.0 M KOH + seawater.

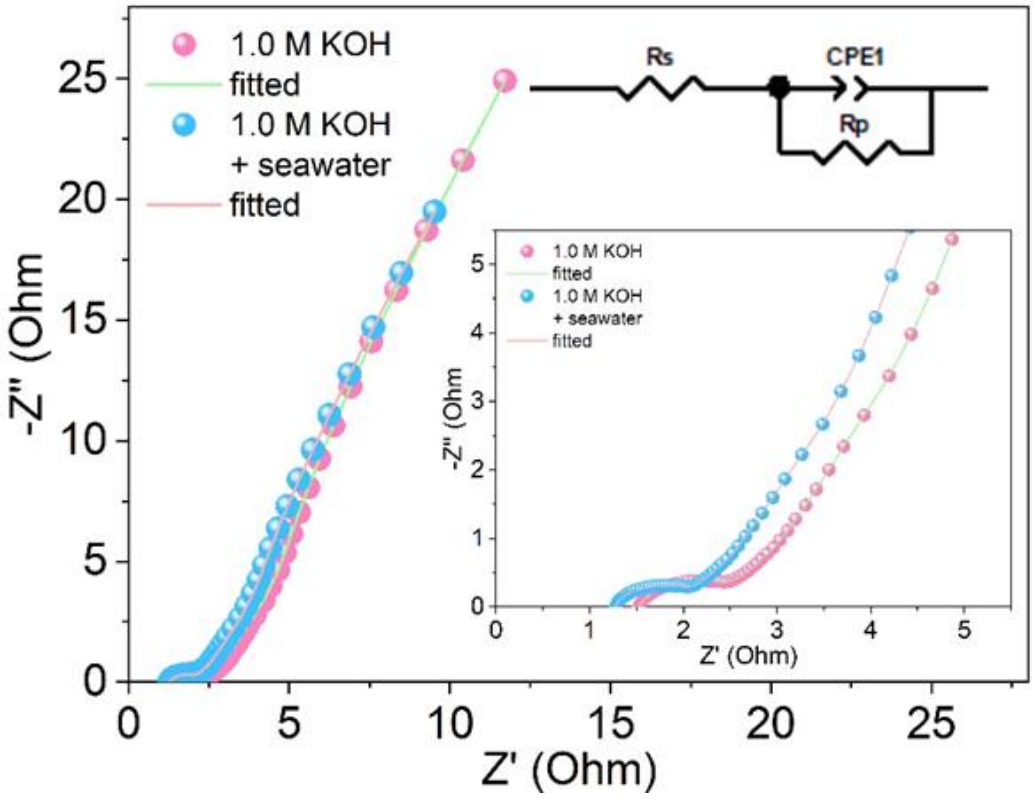

Fig. S17. EIS spectra of FeP@CNT-900-2 in the electrolytes of 1.0 M KOH and 1.0 M KOH + seawater.

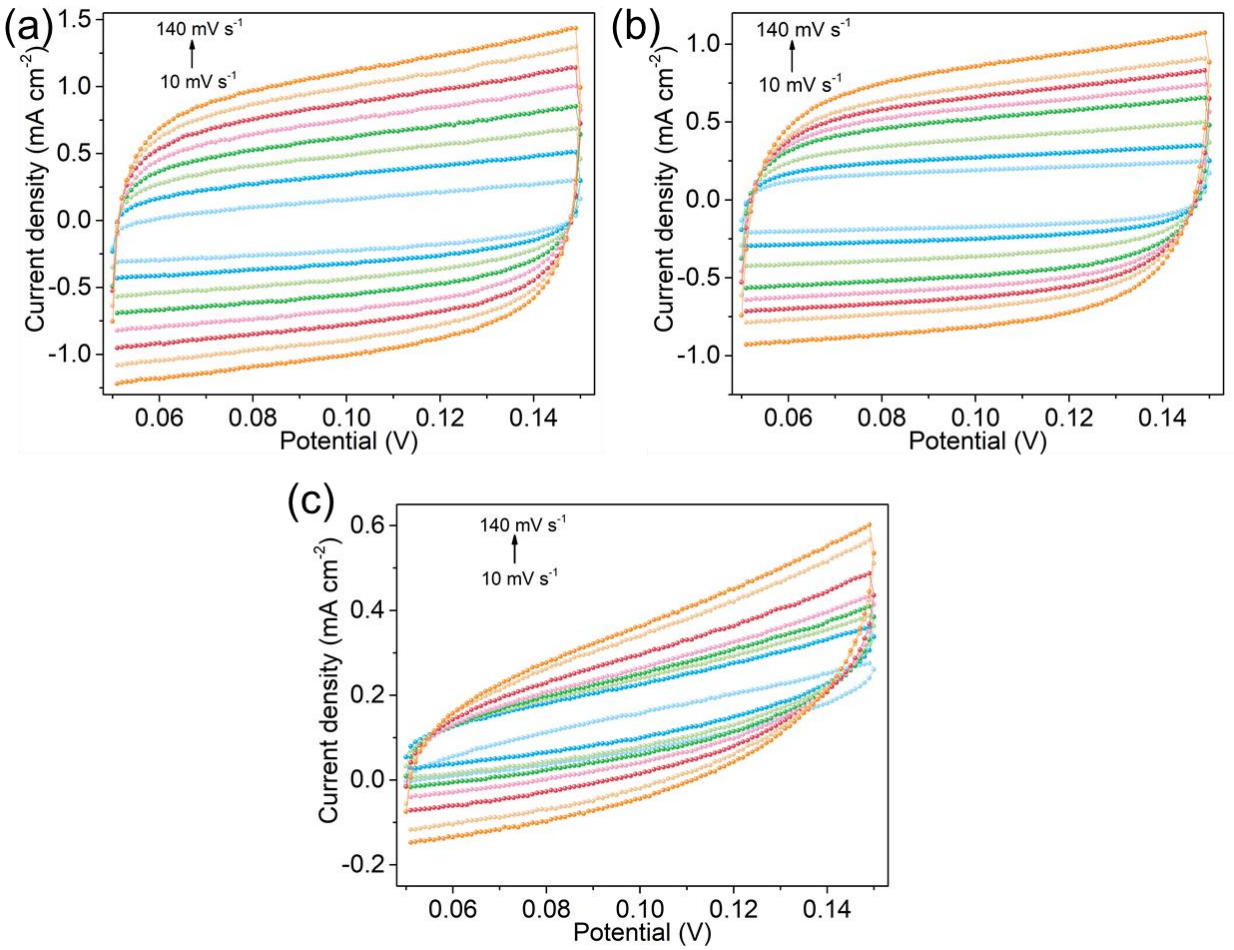

Fig. S18. Double-layer capacitance measurements for determining the ECSA of (a) FeP@CNT-900-2, (b) Fe@C-900, and (c) ZnFe-MOF.

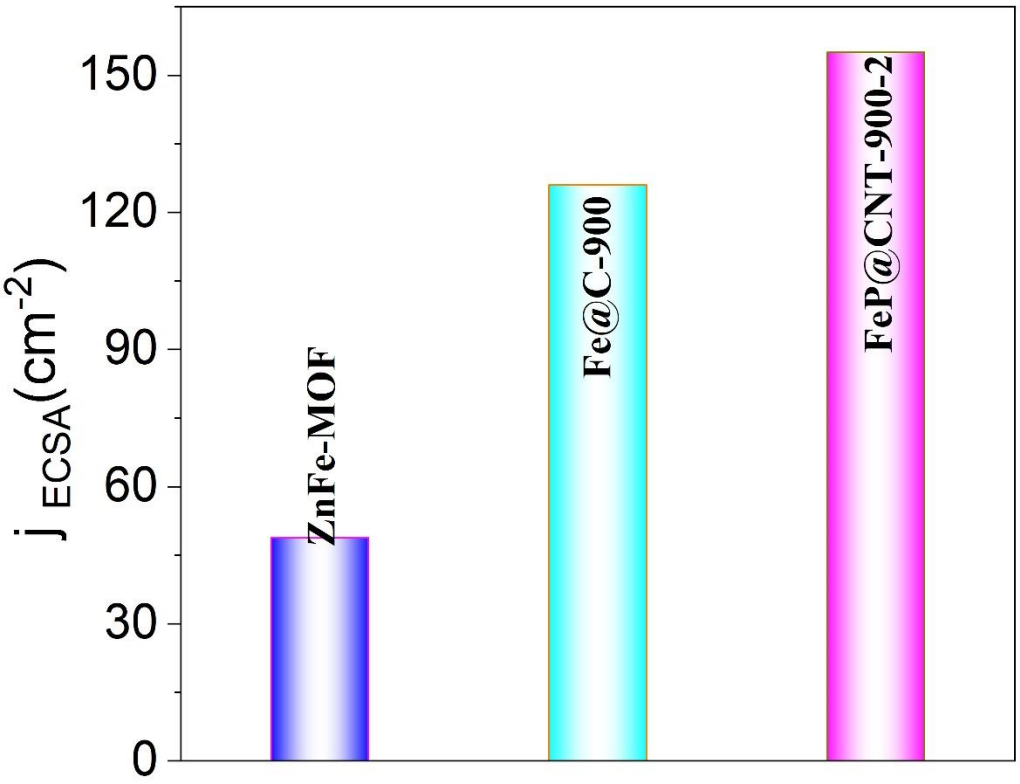

Fig. S19. ECSA of the different electrode materials.

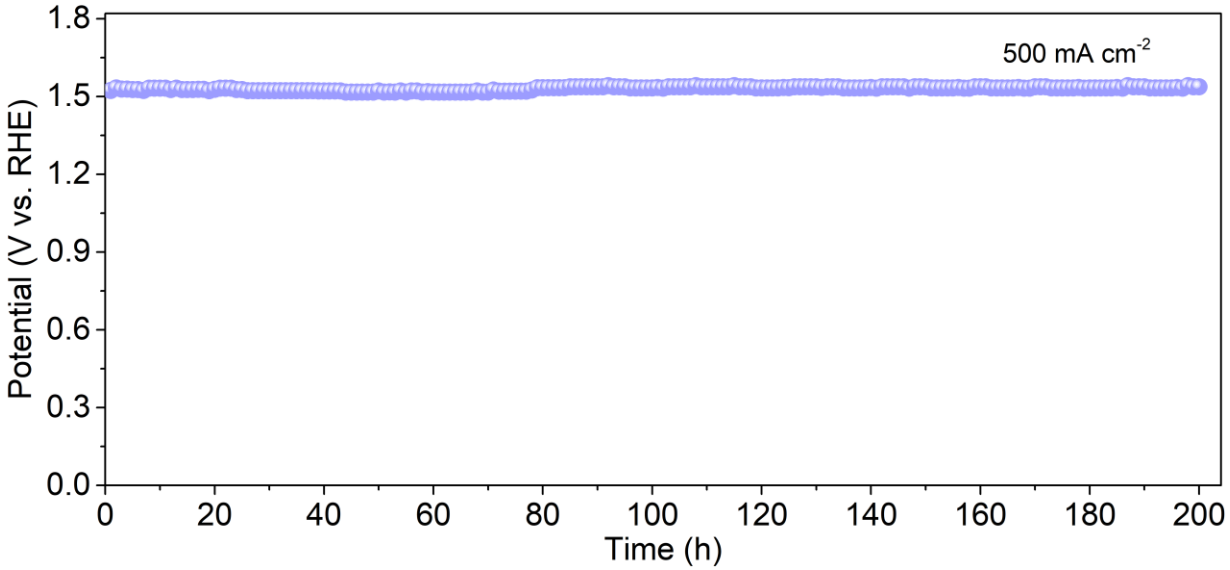

Fig. S20. OER chronoamperometry stability in 1.0 M KOH + seawater at 500 mA cm^{-2} using FeP@CNT-900-2.

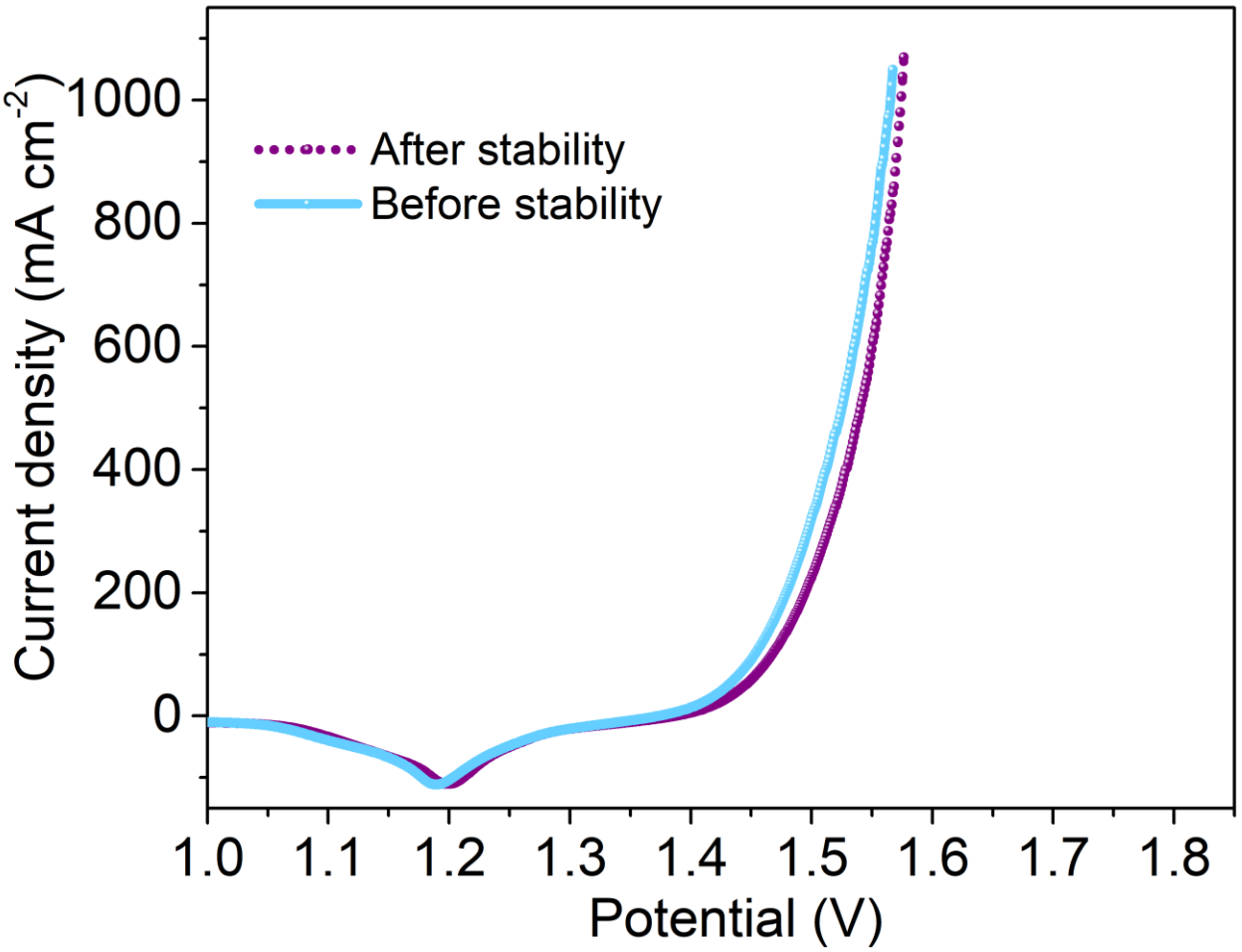

Fig. S21. LSV curve before and after 200 h of stability in alkaline seawater.

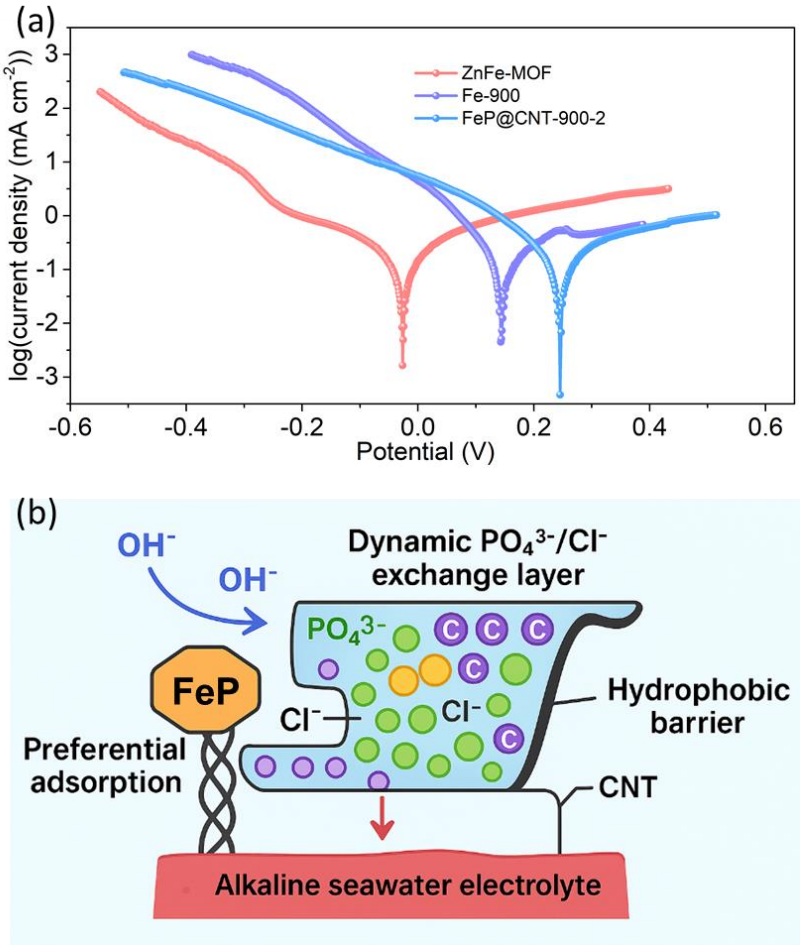

Fig. S22. (a) Tafel polarization curves of the three different electrodes in alkaline seawater and (b) dynamic OH^--anchored phosphate shield mechanism.

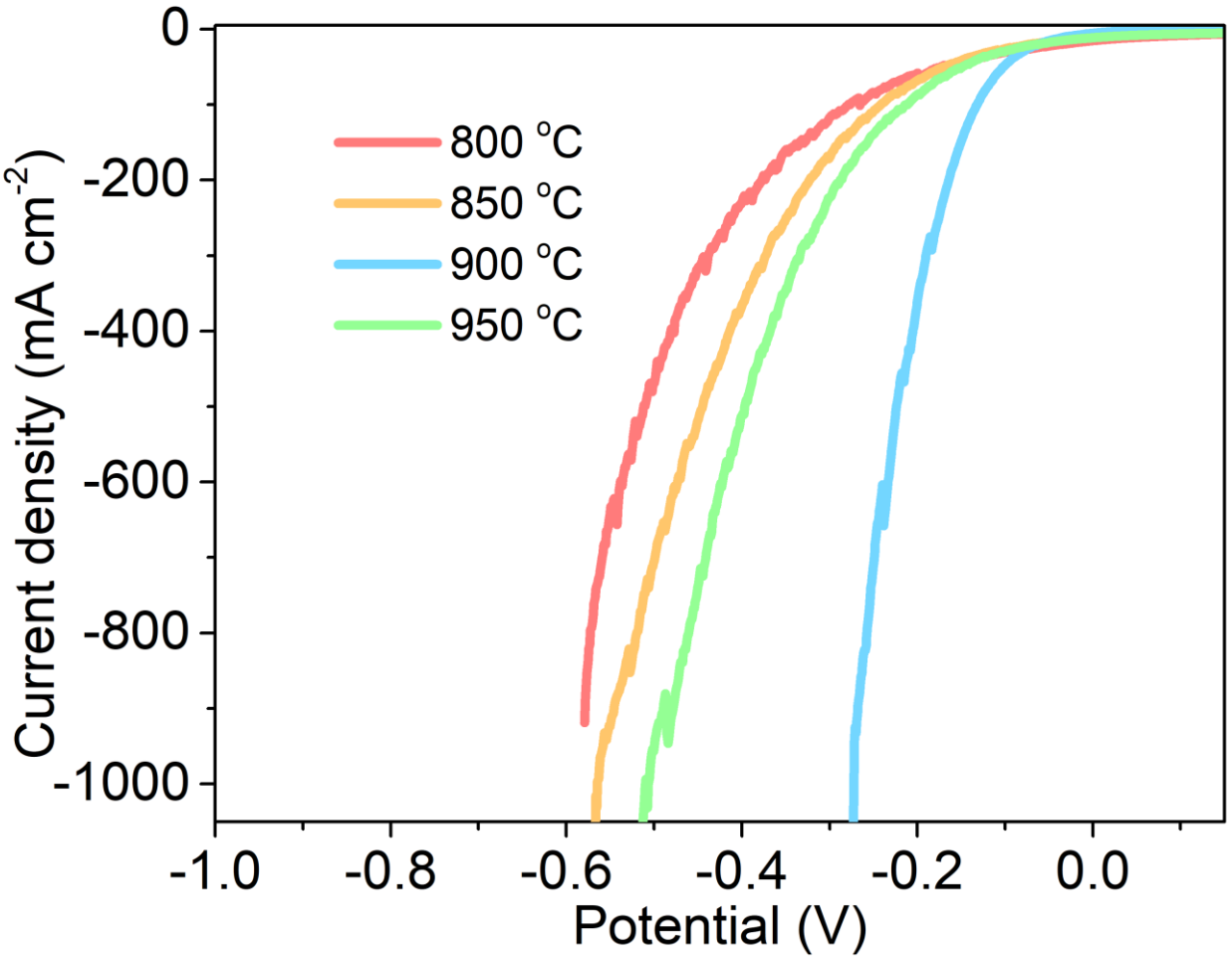

Fig. S23. LSV HER curves of FeP@CNT electrodes fabricated at different temperatures in alkaline seawater.

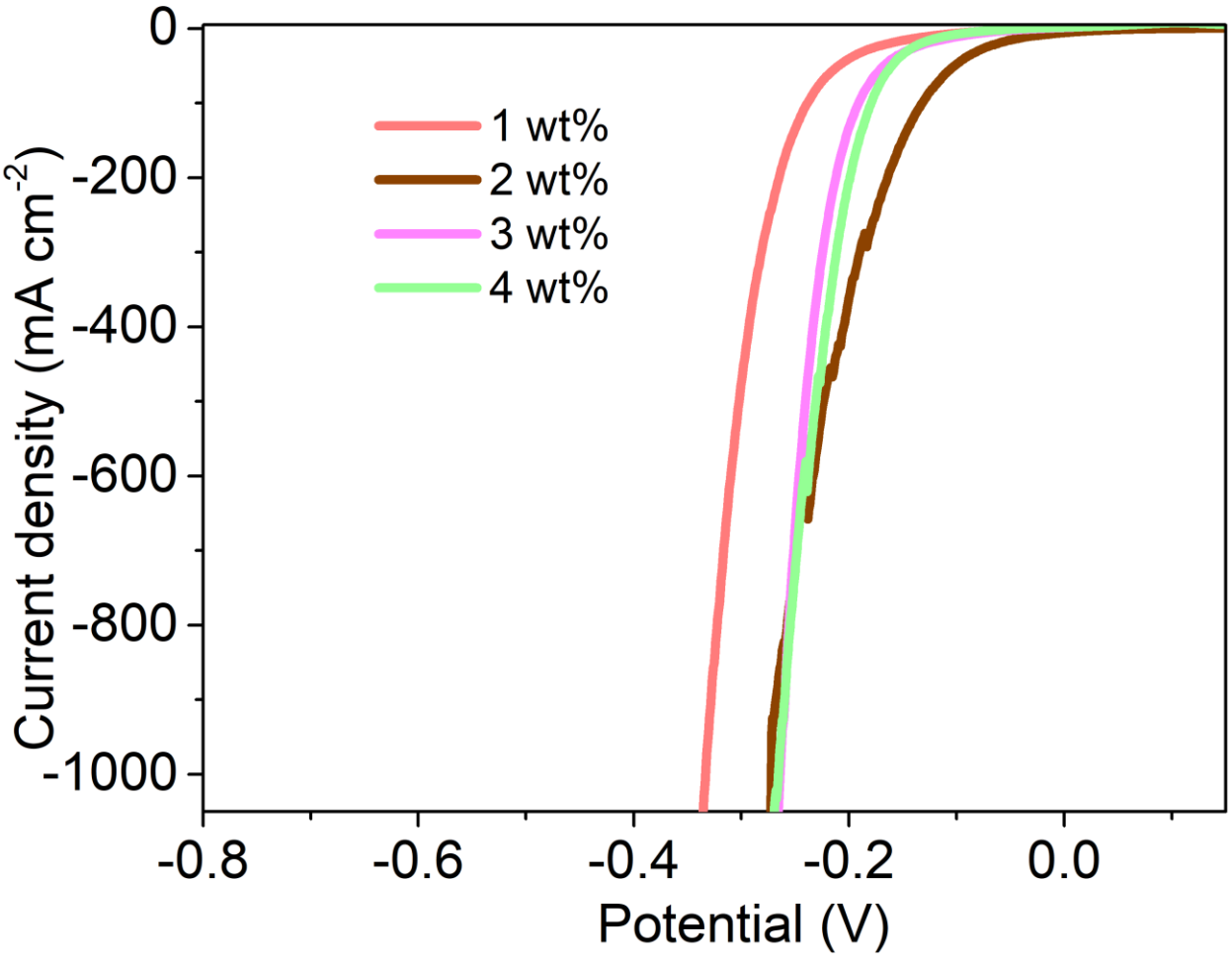

Fig. S24. LSV-HER curves of FeP@CNT electrodes fabricated at different wt.% of NaH_2PO_4.

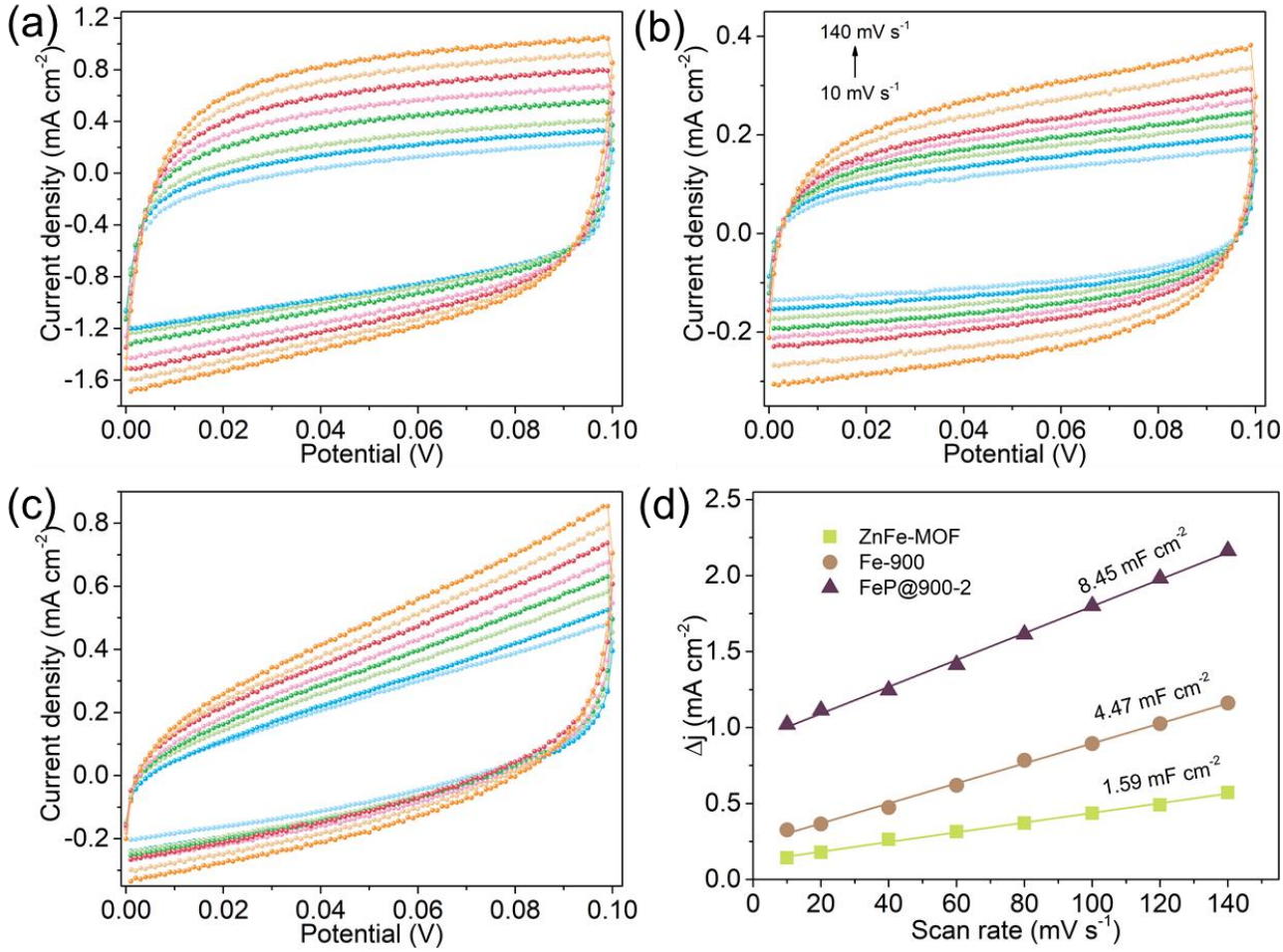

Fig. S25. Double-layer capacitance measurements for determining the ECSA of (a) Fep@CNT-900-2, (b) Fe@900, (c) ZnFe-MOF, and C_{dl} plots.

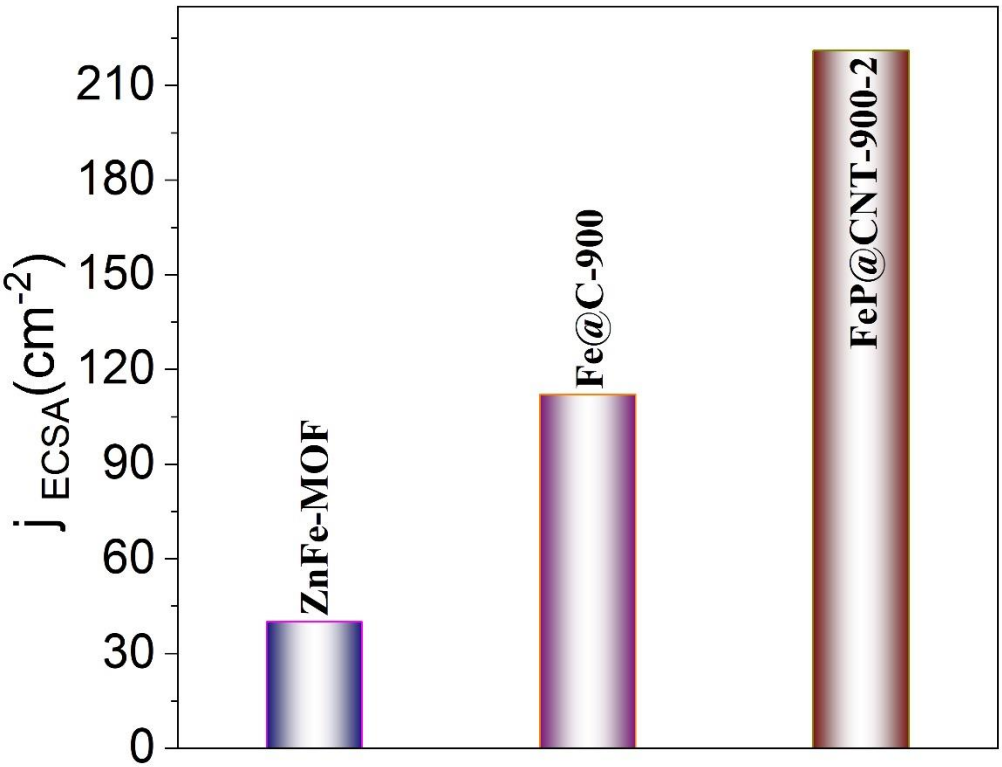

Fig. S26. ECSA of the different electrode materials.

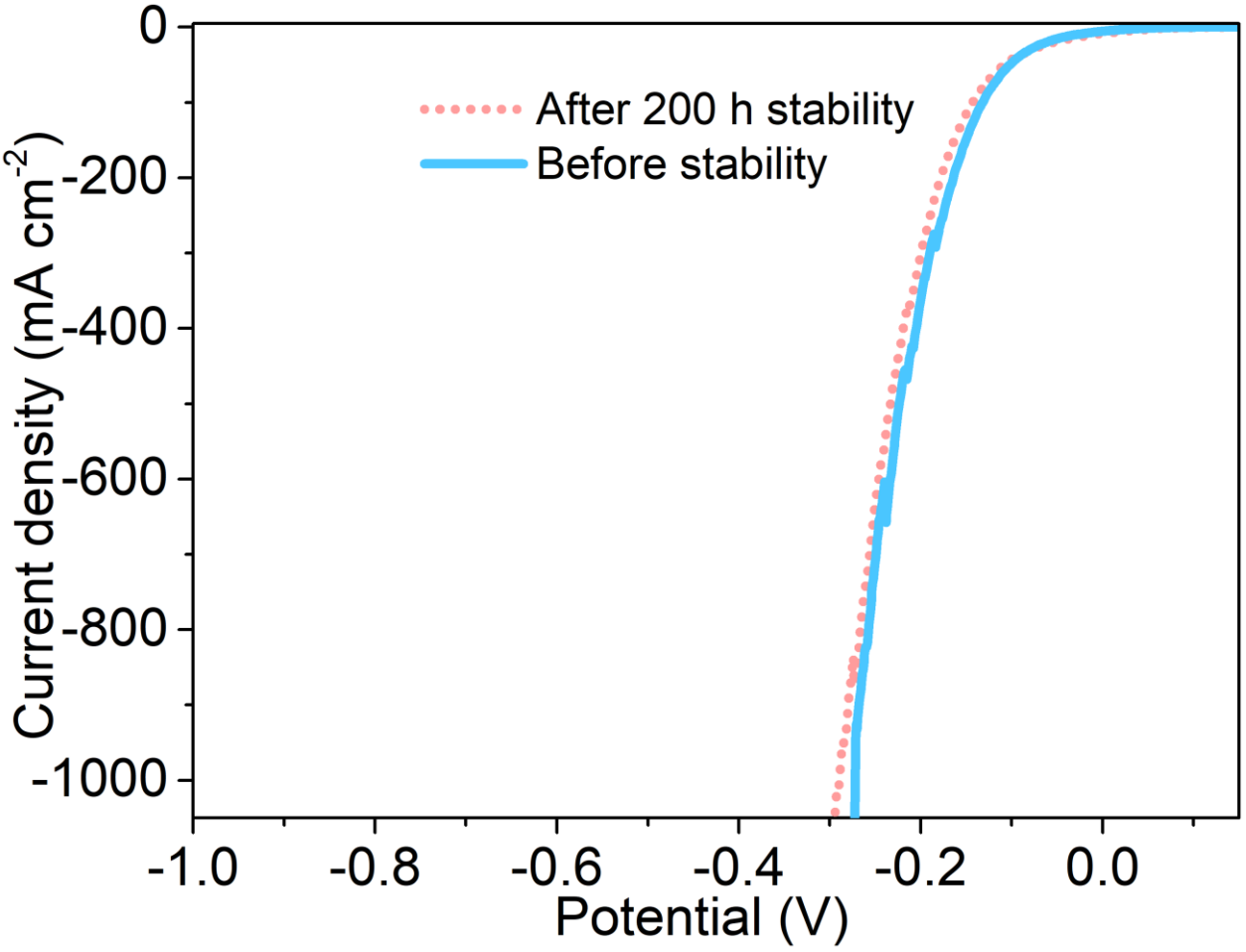

Fig. S27. LSV-HER curve before and after 200 h stability in alkaline seawater.

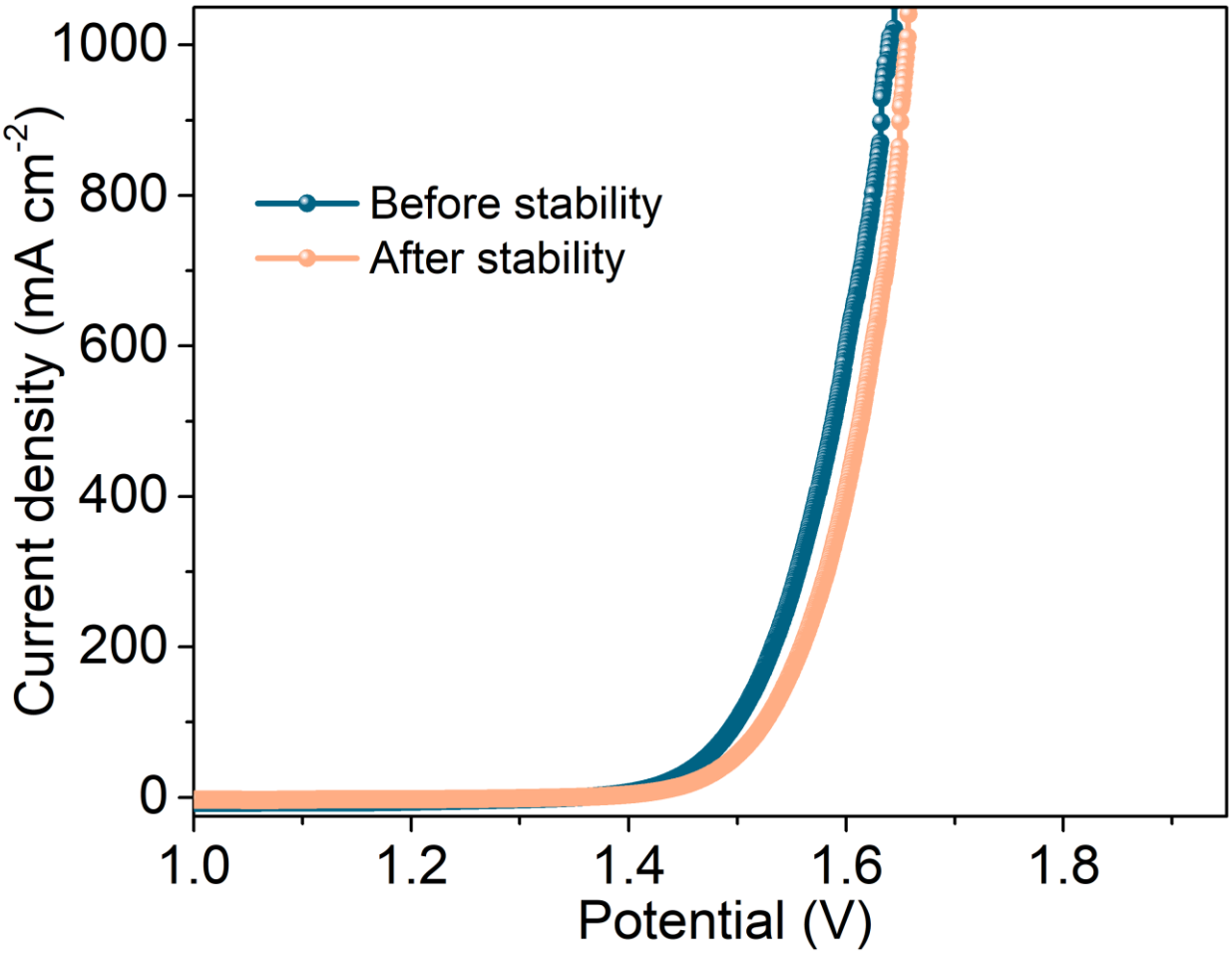

Fig. S28. LSV curve before and after 1000 h overall stability in alkaline seawater.

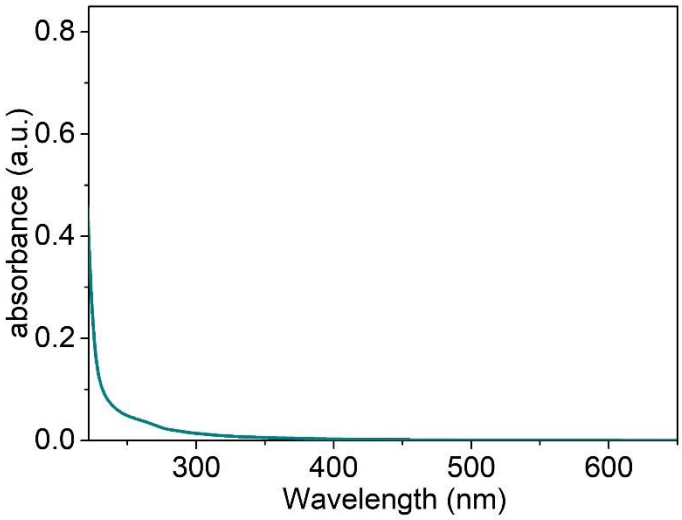

Fig. S29. The UV-vis absorption spectra of the prepared electrolytes from 1.0 M KOH + seawater after anodic oxidation.

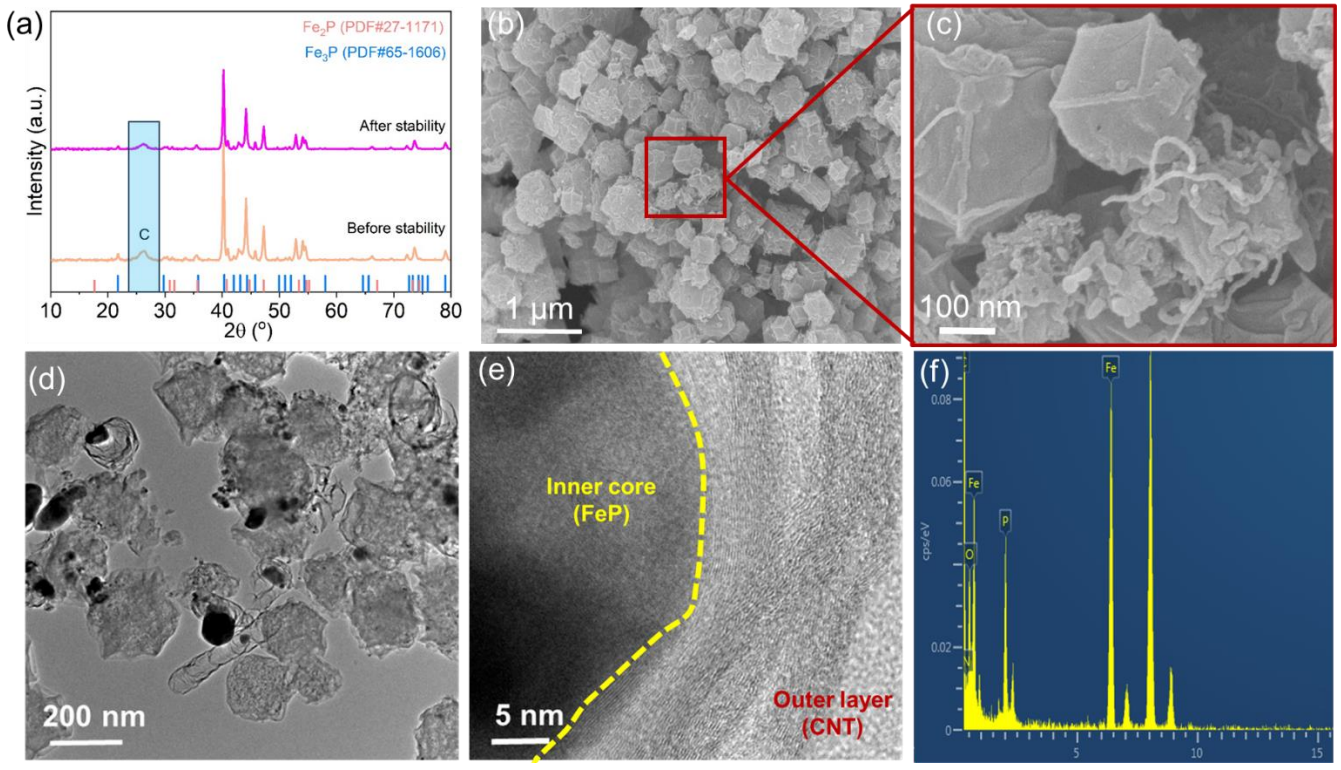

Fig. S30. (a) XRD pattern, (b,c) FE-SEM images, (d,e) TEM and HR-TEM images, and (e) TEM-EDS analysis of post FeP@CNT-900 after 1000 h overall seawater splitting.

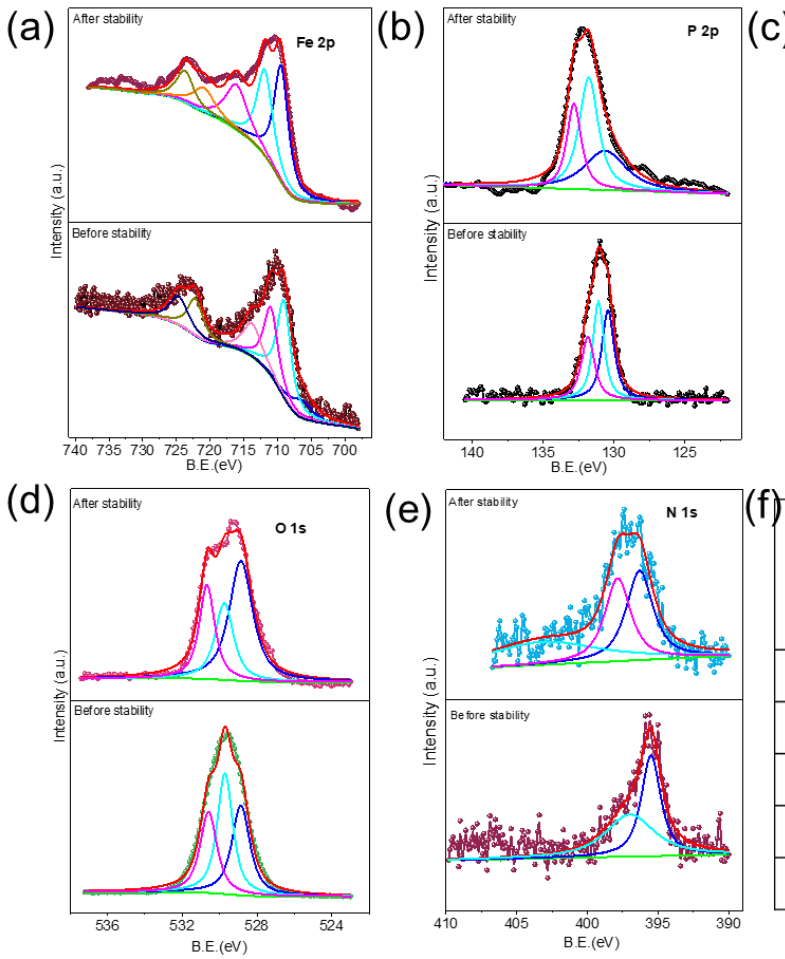

(f)

Elements	Before	After
	Atomic %	Atomic %
C 1s	47.00	80.83
N 1s	02.37	03.51
O 1s	42.14	10.44
P 2p	04.81	02.04
Fe 2p	03.68	03.18

Fig. S31. High-resolution XPS spectra (a) Fe 2p, (b) P 2p, (c) C 1s, (d) O 1s, (e) N 1s, and comparison table for before and after 1000 h stability in seawater electrolysis (FeP@CNT-900-2).

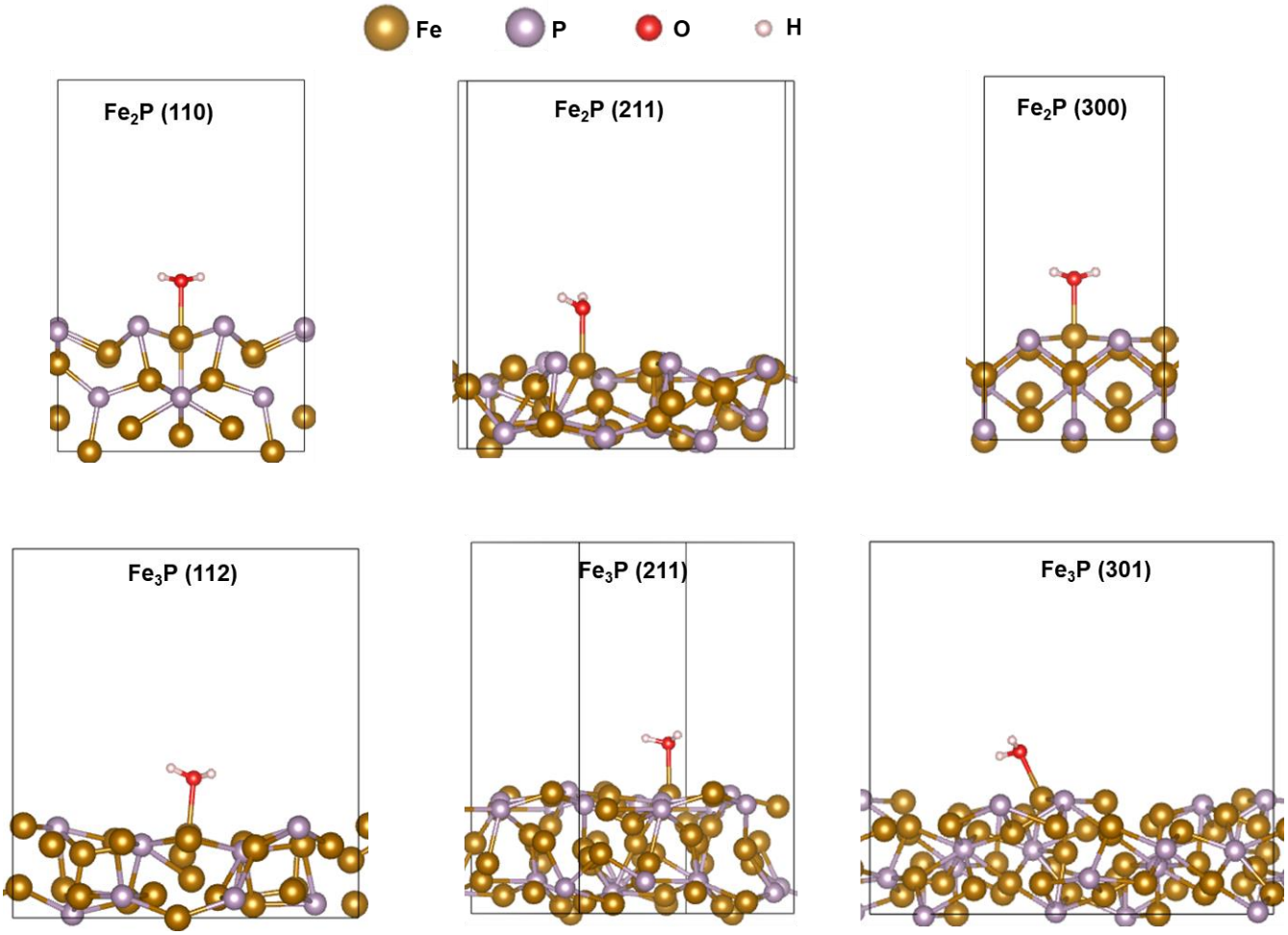

Fig. S32. Atomic configuration of H_2O adsorption on the surface of Fe_2P and Fe_3P.

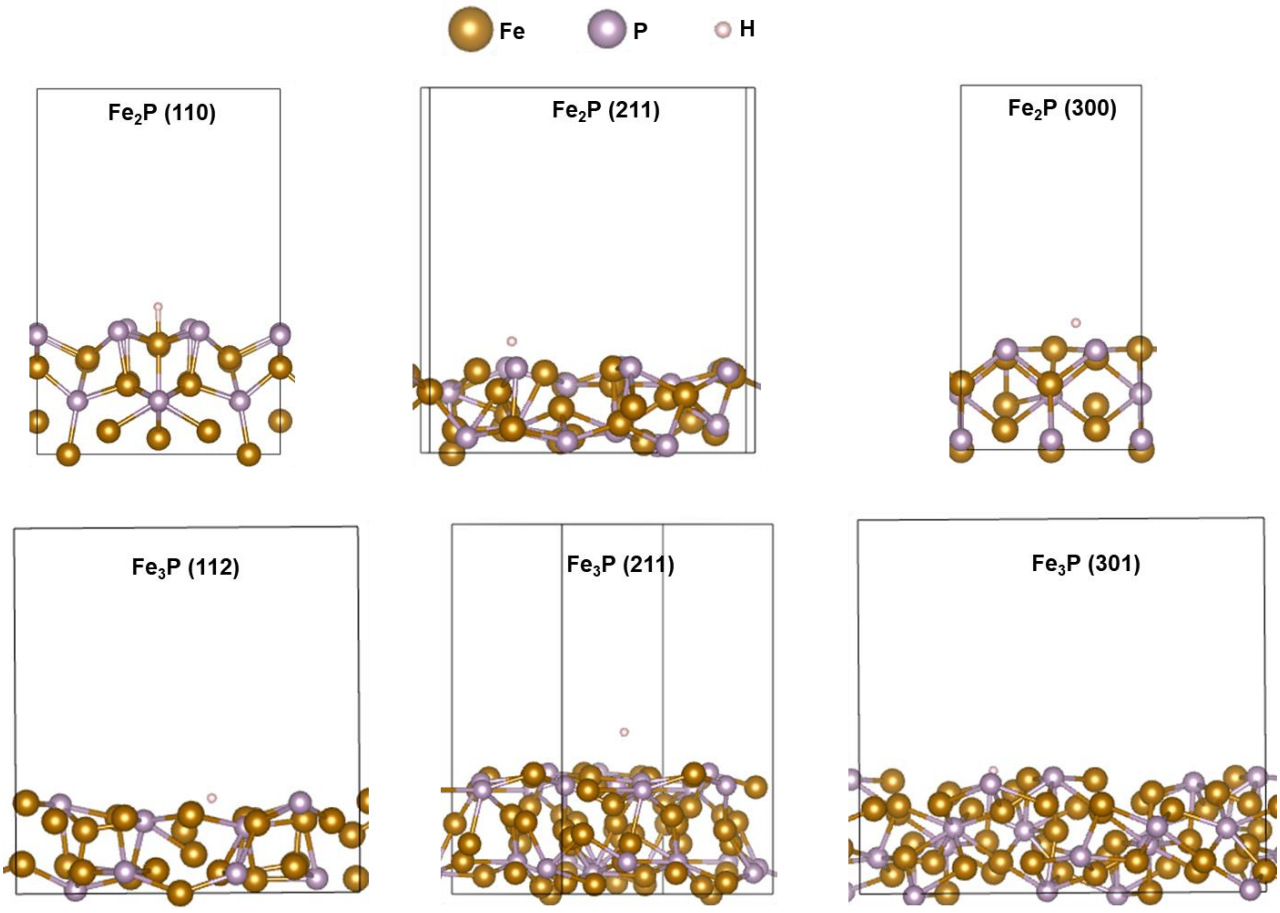

Fig. S33. Atomic configuration of H adsorption on the surface of Fe_2P and Fe_3P.

Table S1. BET specific surface areas and BJH adsorption cumulative volume for Zn-MOF, ZnFe-MOF, and FeP@CNT-900-2 electrode materials.

Materials	**BET ($m^2 g^{-1}$)**	**Pore vol ($cm^3 g^{-1}$)**	**Pore size (nm)**
Zn-MOF	1864.99	0.695	1.51
ZnFe-MOF	1608.21	0.641	2.07
FeP@CNT-900-2	345.63	0.345	2.014

Table S2. Comparison of OER performances for FeP@CNT-900 with other reported electrocatalysts.

Materials	Overpotential (mV)	Tafel (mV/dec)	Stability (h)	Ref.
CoNiFe@NCNTs	341@500	42	24	[6]
Ni_3S_2@CNTs/CC	200@10	61	22	[7]
Cr-FeNi–P/NCN	240@10	72.6	20	[8]
FeNiP/NC	240@10	39.2	45	[9]
Fe-Ni_2P/NC HPs	228@10	33.4	210	[10]
NiMOF-Ni_2P	240@100	63.26	100	[11]
$Co_{0.58}Fe_{0.42}P_y$	232@10	90	10	[12]
FeNi-P@NCNT/CW	180@50	60.9	200	[13]
CoP/Ni_2P/Fe_2P	260@10	65.5	60	[14]
Fe-Co-P	252@50	33	24	[15]
Ni_2P/CoP-NF	238@50	100		[16]
$FeNi_3$-NC-700	262@10	69.4	10	[17]
FeP@CNT-900	184@10	41.2	200	This work

Table S3. Comparison of HER performances for FeP@CNT-900 with other reported electrocatalysts.

Materials	Overpotential (mV)	Tafel (mV/dec)	Stability (h)	Ref.
FeP-Ni_2P-CoP/NF	128@100	78.47	500	[18]
CoNi-P/CDs/NF	45.2@10	69.6	70	[19]
Ni@NP@NCP	80.2	73.68	24	[20]
e-CoNiFeP/NF-2	163	77.9	130	[21]
NiOOH@CoMnS	142@100	51	250	[22]
Se-NiMnSx@SC	146@500	29	500	[23]
V, M (3,6)-NCP	41@10	41.52	100	[24]
$NiMoS_x$@NiMnFe-PBA	71@10	114.7	650	[25]
Ni_3S_2@CoFe-P	153@10	54.8	100	[26]
MoO_2-$Ni_3(PO_4)_2$	258@10	85.32	24	[27]
V-Co_3O_4(Ov)-250	133@10	89.9	100	[28]
PdCo-Co_3S_4	96@10	22.23	10	[29]
FeP@CNT-900	74@10	43.1	200	This work

Table S4. Cell voltage and stability for overall water splitting.

Materials	Potential (V)	Stability (h@mA cm^{-2})	Ref.
$P_{4.8}$-NiFe-400	1.8 @10	500@100	[30]
Ni-Fe-P@CNTs	1.58@10	30@10	[31]
CuCo@NCNT	1.50@10	400@200	[32]
CoP_2/Co_2P@CNT	1.55@10	100@10	[33]
CeNiFe-MOF	1.59@10	515@100	[34]
Fe-NiS	1.53@100	50@1000	[35]
Fe_2P/$Ni_{1.5}Co_{1.5}N$/Ni_2P	1.62@100	40@100	[36]
$NiFeCo(OH)_2$	2.09@500	100@500	[37]
$Ni_{0.8}Fe_{0.2}P$-C	1.56@10	100@10	[38]
Mn-Ni_2P/Fe_2P	2.02@500	120@500	[39]
A-NiFeP/NiP-Fe:25%	1.62@	500@	[40]
Fe-$Ni(OH)_2$@Ni_5P_4	1.70@100	100@200	[41]
Fe-CoP_x/NF	1.54@10	200@100	[42]
NGC-SnSe-P	1.56@10	5@10	[43]
V-Co_2P@NPPC/3DG	1.52@10	60@50	[44]
FeP@CNT-900-2	1.41@10 1.49@100 1.58@500 1.63@1000	1000@500	This work

References

[1] G. Kresse, J. Furthmüller, Efficiency of ab-initio total energy calculations for metals and semiconductors using a plane-wave basis set, Comput. Mater. Sci. 6 (1996) 15–50. https://doi.org/10.1016/0927-0256(96)00008-0.

[2] G. Kresse, J. Furthmüller, Efficient iterative schemes for *ab initio* total-energy calculations using a plane-wave basis set, Phys. Rev. B 54 (1996) 11169–11186. https://doi.org/10.1103/PhysRevB.54.11169.

[3] J.P. Perdew, K. Burke, M. Ernzerhof, Generalized Gradient Approximation Made Simple [Phys. Rev. Lett. 77, 3865 (1996)], Phys. Rev. Lett. 78 (1997) 1396–1396. https://doi.org/10.1103/PhysRevLett.78.1396.

[4] G. Kresse, D. Joubert, From ultrasoft pseudopotentials to the projector augmented-wave method, Phys. Rev. B 59 (1999) 1758–1775. https://doi.org/10.1103/PhysRevB.59.1758.

[5] H.J. Monkhorst, J.D. Pack, Special points for Brillouin-zone integrations, Phys. Rev. B 13 (1976) 5188–5192. https://doi.org/10.1103/PhysRevB.13.5188.

[6] Y. Wang, P. Yang, Y. Gong, Z. Xiao, W. Xiao, L. Xin, Z. Wu, L. Wang, CoNiFe alloy nanoparticles encapsulated into nitrogen-doped carbon nanotubes toward superior electrocatalytic overall water splitting in alkaline freshwater/seawater under large-current density, J. Chem. Phys. 159 (2023). https://doi.org/10.1063/5.0168354.

[7] R.C. Gotame, Y.R. Poudel, G. Ghimire, R. Pathak, J.W. Elam, J. Watt, W. Kuo, W. Li, Nickel Sulfide-Nanowire-Filled Carbon Nanotubes as an Efficient Overall Water Splitting Electrocatalyst, ACS Electrochemistry 1 (2025) 1125–1140. https://doi.org/10.1021/acselectrochem.5c00007.

[8] Y. Wu, X. Tao, Y. Qing, H. Xu, F. Yang, S. Luo, C. Tian, M. Liu, X. Lu, Cr-Doped FeNi–P Nanoparticles Encapsulated into N-Doped Carbon Nanotube as a Robust Bifunctional Catalyst for Efficient Overall Water Splitting, Advanced Materials 31 (2019). https://doi.org/10.1002/adma.201900178.

[9] Y. Cao, Y. Yan, Y. Wen, M. Cao, Y. Li, H. Xie, W. Gu, Fe-Based Metal Organic Framework-Derived FeNiP/N-Doped Carbon Heterogeneous Core–Shell Structures for Oxygen Evolution, Inorg. Chem. 63 (2024) 3599–3609. https://doi.org/10.1021/acs.inorgchem.3c04512.

[10] Z. Xing, M. Huang, Q. Yao, G. Feng, J. Zhu, Q.-L. Zhu, Z.-H. Lu, Engineering Electronic and Morphological Structure of Metal–Organic-Framework-Derived Iron-Doped Ni 2 P/NC Hollow Polyhedrons for Enhanced Oxygen Evolution, Inorg. Chem. 62 (2023) 11796–11808. https://doi.org/10.1021/acs.inorgchem.3c00963.

[11] Y. Wang, X. Yu, Z. Xia, X. Li, Y. Gao, J. Zhang, W. Feng, X. Zou, Y. Zhao, Strong electronic coupling between Ni-based MOF and Ni2P enables high-efficiency oxygen

evolution reaction for various application scenarios, Chemical Engineering Journal 497 (2024) 154483. https://doi.org/10.1016/j.cej.2024.154483.

[12] S. Liu, X. Cui, Q. Wang, R. Wang, J. Wang, C. Wang, Iron and Oxygen Codoped Cobalt Phosphide Solvothermally Prepared from a Metal–Organic Framework for Oxygen Evolution, The Journal of Physical Chemistry C 126 (2022) 15205–15214. https://doi.org/10.1021/acs.jpcc.2c04204.

[13] X. Tao, H. Xu, S. Luo, Y. Wu, C. Tian, X. Lu, Y. Qing, Construction of N-doped carbon nanotube encapsulated active nanoparticles in hierarchically porous carbonized wood frameworks to boost the oxygen evolution reaction, Appl. Catal. B 279 (2020) 119367. https://doi.org/10.1016/j.apcatb.2020.119367.

[14] C. Zhang, Z. Xing, Y. Peng, H. Zhou, L. Zhang, Z.-H. Lu, Inlaying CoP/Ni2P/Fe2P triple heterostructure in MOF-derived carbon nanobox for robust oxygen evolution reaction, Fuel 365 (2024) 131181. https://doi.org/10.1016/j.fuel.2024.131181.

[15] K. Liu, C. Zhang, Y. Sun, G. Zhang, X. Shen, F. Zou, H. Zhang, Z. Wu, E.C. Wegener, C.J. Taubert, J.T. Miller, Z. Peng, Y. Zhu, High-Performance Transition Metal Phosphide Alloy Catalyst for Oxygen Evolution Reaction, ACS Nano 12 (2018) 158–167. https://doi.org/10.1021/acsnano.7b04646.

[16] T. Lin, H. Yang, J. Dong, C. Ni, X. Gao, J. Li, J. Wang, X. He, W. Tan, L. Feng, Z. Li, Constructing Ni2P/CoP heterojunction with stable built-in electric field to boost overall water splitting at industrial current density, Fuel 396 (2025) 135282. https://doi.org/10.1016/j.fuel.2025.135282.

[17] D. Chen, X. Ji, X. Zhou, Q. Sun, S. Xu, L. Mao, Z. Guo, J. Guan, T.-T. Li, J. Qian, MOF-on-MOF-derived hollow FeNi3/N-doped carbon nanorods for efficient oxygen evolution, Chemical Engineering Journal 470 (2023) 144418. https://doi.org/10.1016/j.cej.2023.144418.

[18] Y. Jin, W. Ma, D. Sun, W. Wan, L. Jia, Y. Tu, D. Gong, W. Zhou, H. Chai, Construction of superhydrophilic FeP–Ni 2 P–CoP/NF enriched interfacial heterostructures for promoting efficient and stable overall water splitting under large currents, Inorg. Chem. Front. 12 (2025) 1644–1655. https://doi.org/10.1039/D4QI02841D.

[19] Y. Long, G. Zhao, L. Yang, Y. Xu, C. Xu, Carbon dot embedded CoNi bimetallic phosphide nanorods as an efficient electrocatalyst for overall water splitting, J. Mater. Chem. A Mater. 12 (2024) 33301–33313. https://doi.org/10.1039/D4TA04340E.

[20] P. Yang, Z. Zhang, C. Jin, M. Ren, J. Wang, T. Shi, H. Xing, X. Ji, Synthesis of Urchin-like Ni@NP@NCP Composites with Three Solvothermal Systems for Highly Efficient Overall Seawater Splitting, Langmuir 39 (2023) 6240–6248. https://doi.org/10.1021/acs.langmuir.3c00504.

[21] N. Zhang, J. Sun, J. Yu, Y. Xu, W. Liang, Y. Li, X. Gu, S. Hata, Z. Wu, Y. Wang, Y. Du, Heterogeneous trimetallic phosphides with robust synergistic effect as bifunctional

electrocatalysts for alkaline overall water and seawater splitting, J. Colloid Interface Sci. 698 (2025) 138089. https://doi.org/10.1016/j.jcis.2025.138089.

[22] M.R. Pallavolu, S. Prabu, J.S. Al-Otaibi, S. Pandiaraj, G. Koyyada, T.V.M. Sreekanth, Integrated NiOOH@CoMnS hierarchical nanostructured electrocatalyst for sustainable hydrogen conversion via alkaline seawater electrolysis: synergistic design and mechanistic insights, J. Mater. Chem. A Mater. (2025). https://doi.org/10.1039/D5TA04643B.

[23] S. Prabu, G. Nagaraju, S. Sengodan, K. Chiang, Highly Stable Bifunctional Heterostructured Electrocatalyst Integrated with LDPE-Derived Spherical Carbon for Longevous Alkaline Seawater Splitting, Small 21 (2025). https://doi.org/10.1002/smll.202500453.

[24] T. Bagaria, T. Borgohain, S. Jadhav, T. Das, B. Debnath, Tunable Charge Distribution in Self-Supported NiCoP Through V and Mo Incorporation for Efficient Hydrogen Evolution in all pH Ranges and Alkaline Seawater, Small 21 (2025). https://doi.org/10.1002/smll.202503368.

[25] P. Wang, P. Wang, T. Wu, C. Zhao, Z. Pu, Y. Zhang, Interface Engineering of NiMoS x @NiMnFe Prussian Blue Analogue Nanowires to Efficiently Boost Overall Seawater Splitting at High Current Densities, Adv. Funct. Mater. 35 (2025). https://doi.org/10.1002/adfm.202417924.

[26] Y. Xiao, X. Chen, C. Wang, Y. Yu, Y. Bai, P. Deng, J. Li, Interface Engineering of Ni 3 S 2 @CoFe-P Core-Shell Enhances Alkaline Seawater Hydrogen Evolution Reaction, ChemCatChem (2025). https://doi.org/10.1002/cctc.202500255.

[27] Z. Jin, H. Pang, Y. Cai, M. Yang, J. Xin, H. Ma, X. Wang, G. Yang, W. Sun, W.-Y. Yu, Synergistic Effect of MoO 2 –Ni 3 (PO 4) 2 Heterostructures In Situ Grown on Nickel Foam Enhances the Efficiency of Hydrogen Evolution Reaction in Simulated Seawater, Cryst. Growth Des. 24 (2024) 9097–9109. https://doi.org/10.1021/acs.cgd.4c01122.

[28] W.-J. Xu, S.U. Rahman, Y.-Y. Wang, J.-Y. Dang, X.-Y. Zhang, W.-L. Li, J. Zhang, Defect and doping synergistic optimization for efficient and durable alkaline seawater hydrogen production, J. Colloid Interface Sci. 690 (2025) 137354. https://doi.org/10.1016/j.jcis.2025.137354.

[29] P. Sun, X. Zheng, A. Chen, G. Zheng, Y. Wu, M. Long, Q. Zhang, Y. Chen, Constructing Amorphous-Crystalline Interfacial Bifunctional Site Island-Sea Synergy by Morphology Engineering Boosts Alkaline Seawater Hydrogen Evolution, Advanced Science 11 (2024). https://doi.org/10.1002/advs.202309927.

[30] L. Song, D. Zhang, H. Miao, Y. Shi, M. Wang, L. Zhao, T. Zhan, J. Lai, L. Wang, Interstitial atom-doped NiFe alloy as pre-catalysts boost direct seawater oxygen evolution, Appl. Catal. B 342 (2024) 123376. https://doi.org/10.1016/j.apcatb.2023.123376.

[31] S. Shao, X. Li, R. Guo, J. Wang, M. Sheng, Ni-Fe-P nanoparticles encapsulated in carbon nanotubes supported on carbon cloth for overall water splitting, Mater. Lett. 352 (2023) 135204. https://doi.org/10.1016/j.matlet.2023.135204.

[32] B. Geng, R. Chen, G. Li, K. Liu, Y. Chen, CuCo nanoparticles encapsulated with nitrogen-doped carbon nanotubes for efficient and stable alkaline saline water splitting, Chemical Engineering Journal 521 (2025) 166626. https://doi.org/10.1016/j.cej.2025.166626.

[33] R. Guo, J. Shi, L. Hong, K. Ma, W. Zhu, H. Yang, J. Wang, H. Wang, M. Sheng, CoP_2 /Co_2P Encapsulated in Carbon Nanotube Arrays to Construct Self-Supported Electrodes for Overall Electrochemical Water Splitting, ACS Appl. Mater. Interfaces 14 (2022) 56847–56855. https://doi.org/10.1021/acsami.2c17742.

[34] J. Yang, Y. Shen, J. Xian, R. Xiang, G. Li, Rare-earth element doped NiFe-MOFs as efficient and robust bifunctional electrocatalysts for both alkaline freshwater and seawater splitting, Chem. Sci. 16 (2025) 685–692. https://doi.org/10.1039/D4SC06574C.

[35] C. Yang, K. Dong, L. Zhang, X. He, J. Chen, S. Sun, M. Yue, H. Zhang, M. Zhang, D. Zheng, Y. Luo, B. Ying, Q. Liu, A.M. Asiri, M.S. Hamdy, X. Sun, Improved Alkaline Seawater Splitting of NiS Nanosheets by Iron Doping, Inorg. Chem. 62 (2023) 7976–7981. https://doi.org/10.1021/acs.inorgchem.3c00836.

[36] F. Zhang, Y. Liu, F. Yu, H. Pang, X. Zhou, D. Li, W. Ma, Q. Zhou, Y. Mo, H. Zhou, Engineering Multilevel Collaborative Catalytic Interfaces with Multifunctional Iron Sites Enabling High-Performance Real Seawater Splitting, ACS Nano 17 (2023) 1681–1692. https://doi.org/10.1021/acsnano.2c11844.

[37] Y. Yu, W. Zhou, X. Zhou, J. Yuan, X. Zhang, L. Wang, J. Li, X. Meng, F. Sun, J. Gao, G. Zhao, The Corrosive Cl^--Induced Rapid Surface Reconstruction of Amorphous NiFeCoP Enables Efficient Seawater Splitting, ACS Catal. 14 (2024) 18322–18332. https://doi.org/10.1021/acscatal.4c05704.

[38] X. Zhang, X.-R. Shi, P. Wang, Z. Bao, M. Huang, Y. Xu, S. Xu, Bio-inspired design of NiFeP nanoparticles embedded in (N,P) co-doped carbon for boosting overall water splitting, Dalton Transactions 52 (2023) 6860–6869. https://doi.org/10.1039/D3DT00583F.

[39] Y. Luo, P. Wang, G. Zhang, S. Wu, Z. Chen, H. Ranganathan, S. Sun, Z. Shi, Mn-doped nickel–iron phosphide heterointerface nanoflowers for efficient alkaline freshwater/seawater splitting at high current densities, Chemical Engineering Journal 454 (2023) 140061. https://doi.org/10.1016/j.cej.2022.140061.

[40] S.-Y. Lu, L. Wang, C. Wu, J. Zhang, W. Dou, T. Hu, R. Wang, Y. Liu, Q. Yang, M. Jin, Adjustable composition of self-supported amorphous Ni–Fe–P nanosheet decorated NiP microspheres for efficient and stable overall alkaline freshwater/seawater splitting, Inorg. Chem. Front. 11 (2024) 3187–3199. https://doi.org/10.1039/D4QI00582A.

[41] L. Kang, D. Cai, S. Geng, H. Li, J. Zhang, K. Wang, S. Song, Y. Wang, Improved Activity and Corrosion Resistance in Seawater Oxidation: Harnessing the Synergy between the Phosphide Layer and Nickel–Iron Hydroxide, Energy & Fuels 39 (2025) 8612–8625. https://doi.org/10.1021/acs.energyfuels.5c00943.

[42] B. Sun, L. Wang, C. Li, X. Meng, Electronic Regulation by Fe-Doped CoP_x Hydrophilic Self-Supported Nanorod Arrays as Bifunctional Electrocatalysts for Superior Overall Seawater Splitting, ACS Sustain. Chem. Eng. 13 (2025) 1118–1129. https://doi.org/10.1021/acssuschemeng.4c09394.

[43] M. Pahuja, S.G. Dastider, Jyoti, K. Alam, S. Rani, S. Das, R. Urkude, M. Afshan, D. Rani, N. Chaudhary, S.A. Siddiqui, S. Riyajuddin, R. Ghosh, K. Mondal, K. Ghosh, Harvesting Green Hydrogen from the Deep Blue: Seawater-Compatible SnSe-P Decorated Graphene-CNTs Based Electrocatalyst Under Universal pH, Small 20 (2024). https://doi.org/10.1002/smll.202406113.

[44] S. Jia, Y. Gao, X. Ma, Y. Cao, Q. Huang, Q. Zhang, Z. Wang, Y. Wang, Y. Li, D. Li, R. Chang, Y. Mu, V-doped Co_2P Anchored on the N–P-Doped Three-Dimensional Covalently Cross-Linked Graphene As a Hydrogen Evolution Reaction Catalyst for Alkaline Water/Seawater Splitting, Inorg. Chem. 64 (2025) 6147–6158. https://doi.org/10.1021/acs.inorgchem.4c05537.